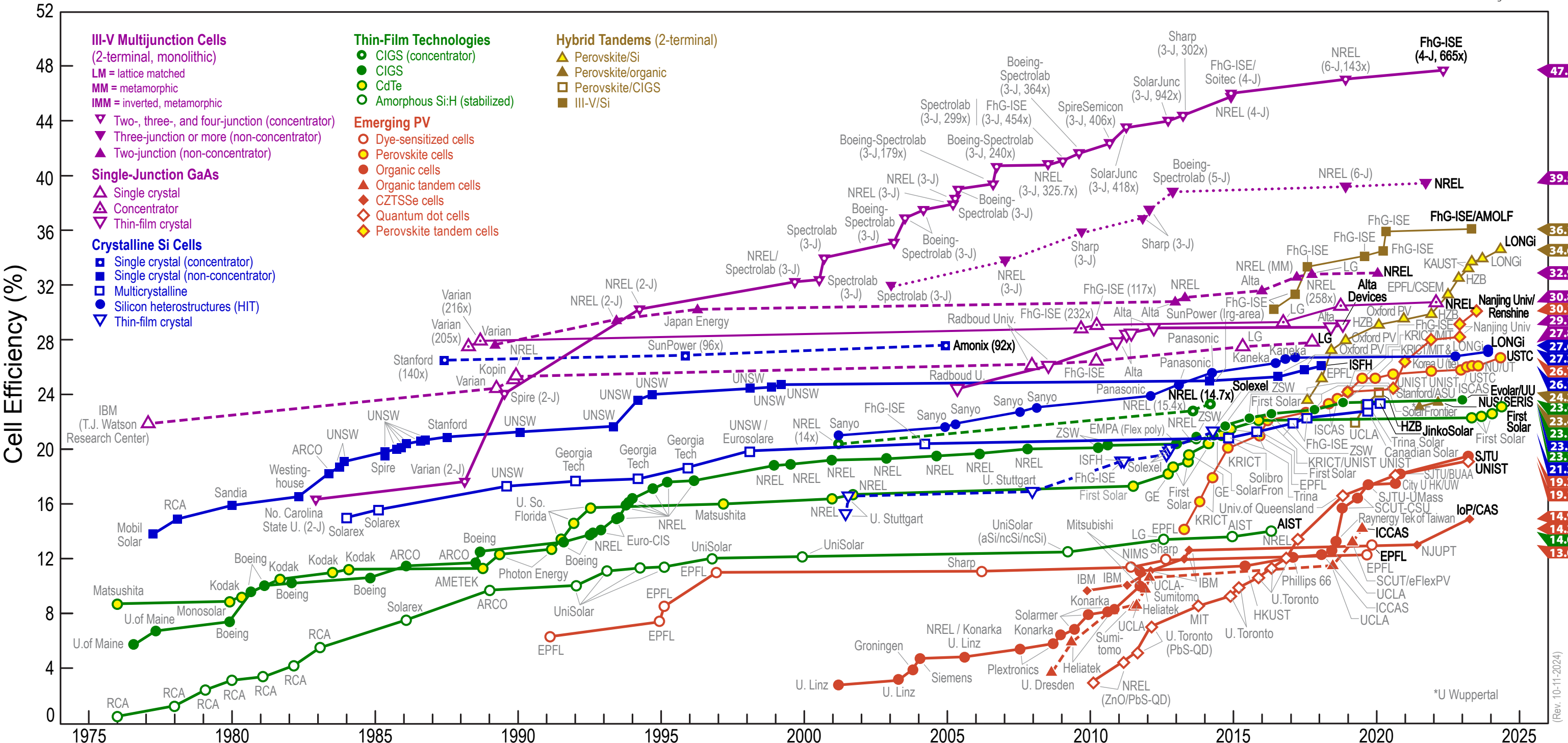


Best Research-Cell Efficiencies



Supplementary information

Intact 2D/3D halide junction perovskite solar cells via solid-phase in-plane growth

In the format provided by the
authors and unedited

Supplementary Information for

Intact 2D/3D halide junction perovskite solar cells via solid-phase in-plane growth

Authors: Yeoun-Woo Jang^{1,3†}, Seungmin Lee^{2†}, Kyung Mun Yeom², Kiwan Jeong¹, Kwang Choi², Mansoo Choi^{1,3*}, and Jun Hong Noh^{2,4*}.

Affiliations:

¹ Global Frontier Center for Multiscale Energy Systems, Seoul National University, Seoul 08826, Republic of Korea

² School of Civil, Environmental and Architectural Engineering, Korea University, Seoul 02841, Republic of Korea

³ Department of Mechanical and Aerospace Engineering, Seoul National University, Seoul 08826, Republic of Korea

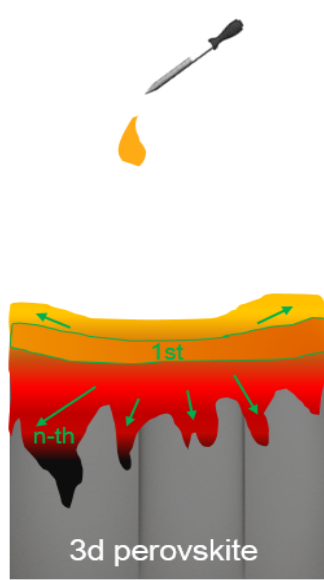
⁴ KU-KIST Green School Graduate School of Energy and Environment, Korea University, Seoul 02841, Republic of Korea

*Corresponding author: Email: junhnoh@korea.ac.kr (J. H. N.) and mchoi@snu.ac.kr (M. C.)

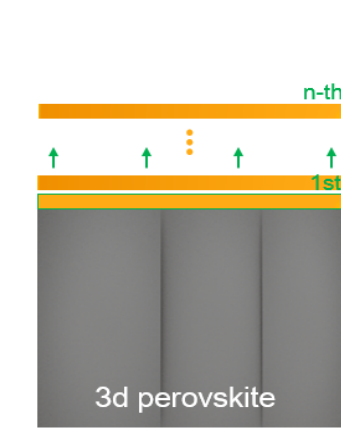
[†]These authors contributed equally to this work

Supplementary Table 1. Comparison of SIG and solution process methods for fabricating a 2D perovskite layer on a 3D perovskite.

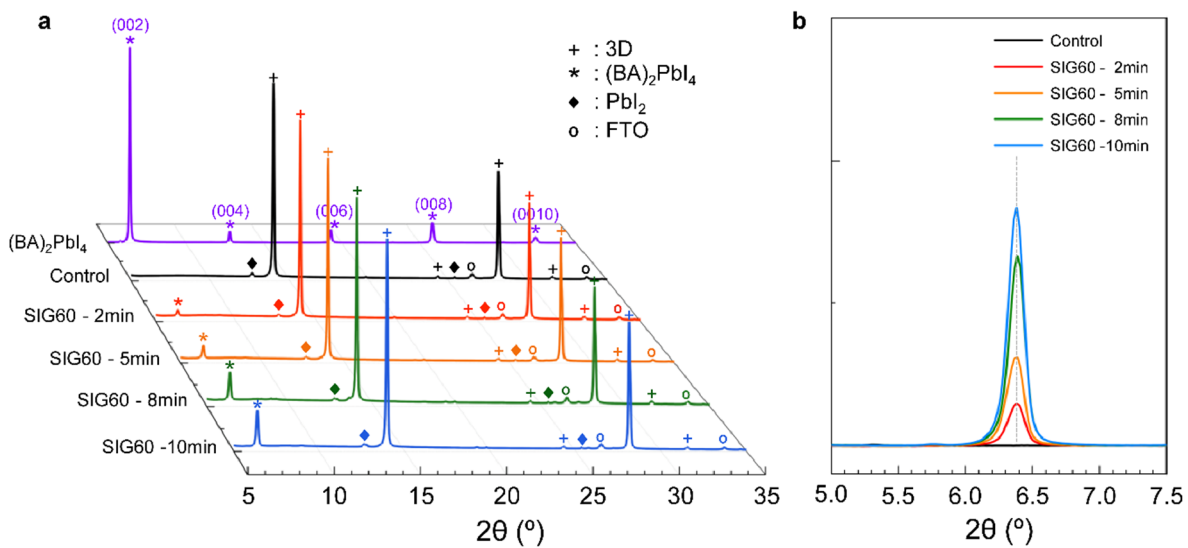
	2D perovskite precursor solution post-deposition	2D perovskite Solid-phase In-plane Growth (SIG) process
State of precursor	Liquid	Solid
Formation mechanism	$\text{BAI}_{(\text{aq})} + \Delta_1 \rightarrow (\text{BA})_2\text{PbI}_4_{(\text{s})} + \Delta_2$ <small>Δ_1: material from 3D perovskite surface Δ_2: material of uncertain composition</small>	$(\text{BA})_2\text{PbI}_4_{(\text{s})} \rightarrow (\text{BA})_2\text{PbI}_4_{(\text{s})}$
Strengths	Thin layer processible Surface passivation	Identified compartmental film Perfect stoichiometry Multiple layer processible Easy thickness control
After process iteration	Fusion with 3D perovskite substrate	Intact multiple layer film formation with the desired thickness



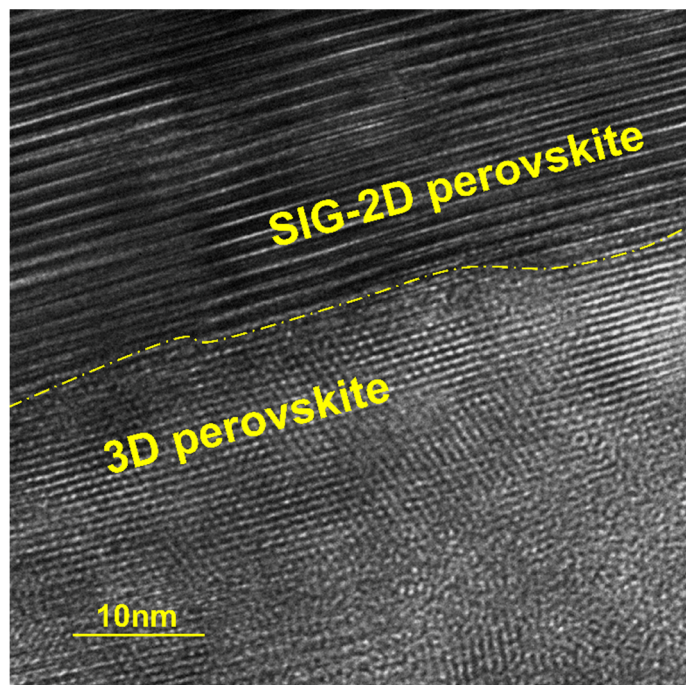
liquid-state deposition



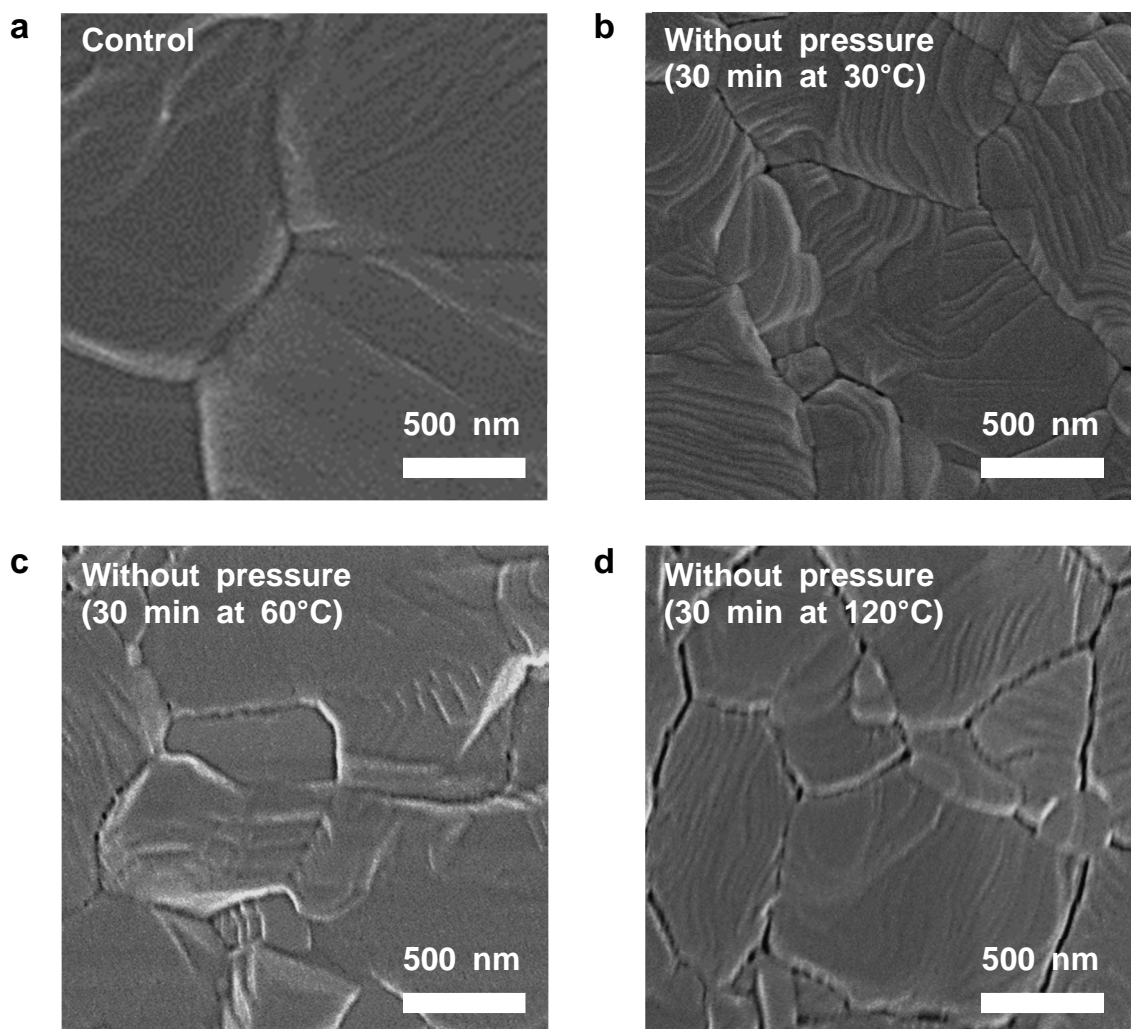
solid-state deposition



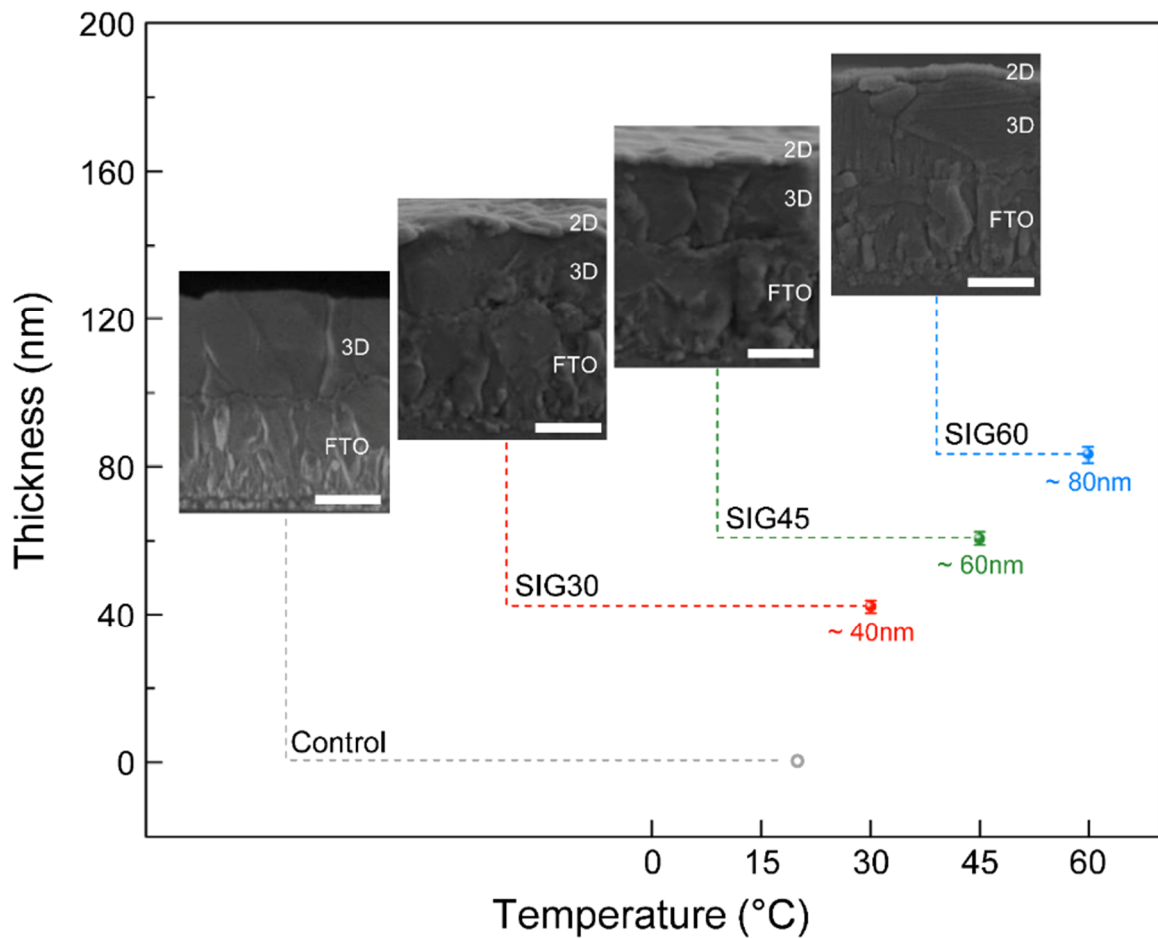
Supplementary Figure 1. Time-dependent X-ray diffraction patterns of SIG60 films. **a**, XRD patterns of SIG60 films according to the SIG process time. **b**, Trend of the $(\text{BA})_2\text{PbI}_4$ (002) peak over time. As the time of the SIG method increased, the intensity of the $(\text{BA})_2\text{PbI}_4$ peak was enhanced. Indexes of the 3D film, $(\text{BA})_2\text{PbI}_4$ film and FTO were confirmed through previous studies^{1,2}, and for the index of PbI_2 , JCPSD #07-0235 was used.



Supplementary Figure 2. High-resolution transmission electron microscopy image at the junction between the 3D material and SIG-(BA)₂PbI₄ of the SIG60 film.

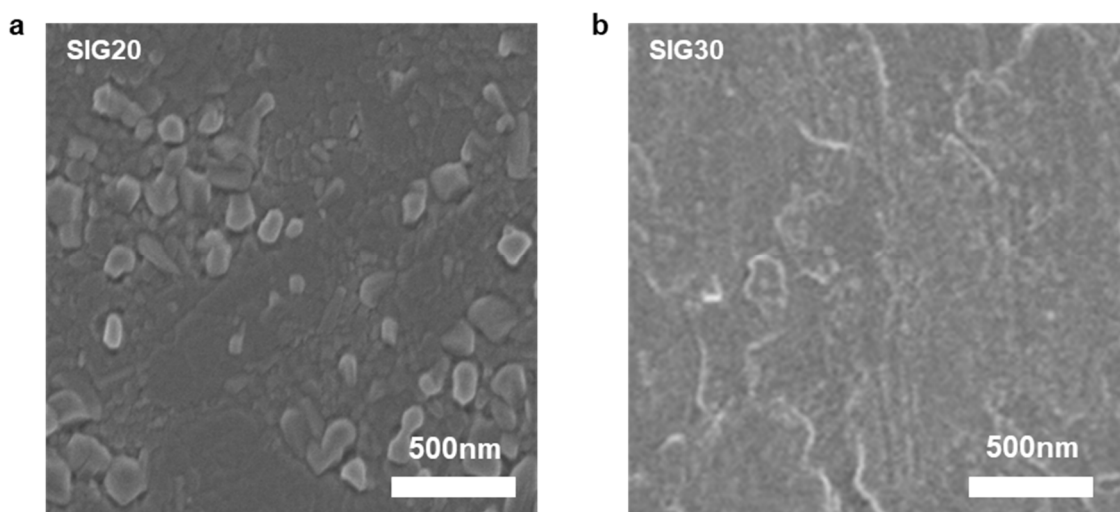


Supplementary Figure 3. Temperature-dependent scanning electron microscopy images of SIG films without pressure. **a.** Scanning electron microscope (SEM) image of the control 3D film. **b-d,** SEM images of SIG films without additional pressure for 30 min at different temperatures.



Supplementary Figure 4. SIG-(BA)₂PbI₄ thickness as a function of SIG temperature.

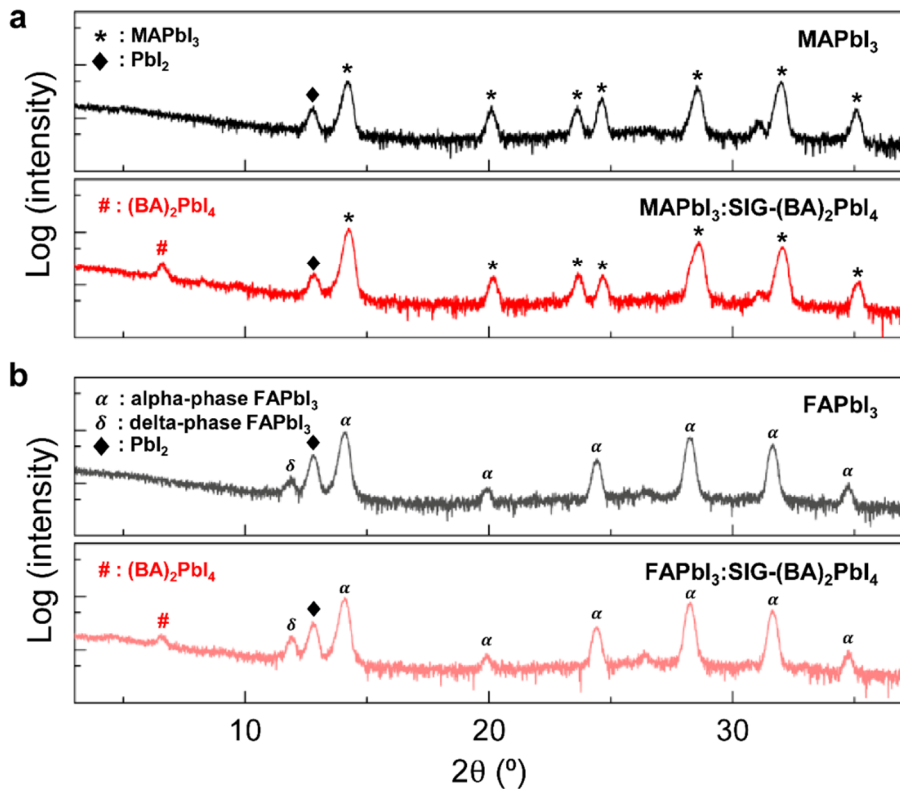
The thickness of $(\text{BA})_2\text{PbI}_4$ fabricated at each SIG temperature. All thicknesses of $(\text{BA})_2\text{PbI}_4$ were observed through SEM images. Inserts are representative images of each SIG film. Error bars show the lower and upper thicknesses of $(\text{BA})_2\text{PbI}_4$ at each SIG temperature. All scale bars: 500 nm.



Supplementary Figure 5. Lower temperature limit of SIG-(BA)₂PbI₄ on the surface of the 3D film. a-b. SEM images of the SIG film surface after 12 h under a 60 MPa pressure at 20°C (a) and 30°C (b).

Supplementary Table 2. Position of the (002) peak of the (BA)₂PbI₄ films and its FWHM in XRD patterns. The XRD pattern of a pure (BA)₂PbI₄ film fabricated by spin coating on ITO showed an FWHM of 0.105° for the (002) peak. SIG films with (BA)₂PbI₄, even for different temperature conditions (30°C, 45°C, and 60°C), showed FWHMs of 0.152 ° to 0.167 ° at the position corresponding to the (002) peak of pure (BA)₂PbI₄. The small FWHM of 0.15° means that the SIG process can induce a highly crystalline (BA)₂PbI₄ film on the 3D perovskite surface compared to conventional processes.

Film type	Film structure	Peak position (2θ)	FWHM (°)
(BA) ₂ PbI ₄	ITO/2D	6.41	0.105
SIG30	FTO/3D:SIG-2D	6.38	0.167
SIG45	FTO/3D:SIG-2D	6.38	0.153
SIG60	FTO/3D:SIG-2D	6.39	0.152



Supplementary Figure 6. XRD patterns of 3D and 3D:SIG-(BA)₂PbI₄ in compliance with the 3D perovskite composition. Similar to (FAPbI₃)_{0.95}(MAPbBr₃)_{0.05}, after the SIG process, a typical (BA)₂PbI₄ peak was found near 6.4° in either the (a) MAPbI₃ or (b) FAPbI₃ composition. Indexes of FAPbI₃, MAPbI₃, and (BA)₂PbI₄ films and FTO were confirmed through previous studies²⁻⁵, and for the index of PbI₂, JCPSD #07-0235 was used.

Supplementary Note 1

Three mechanisms determine PL decay: first-order (trap-assisted nonradiative); second-order (radiative); and third-order (Auger) recombination, and their contributions depend on the intensity of the excitation laser fluence⁶. To elucidate the recombination pathways of a halide perovskite over a range of excitation fluence, the carrier kinetics can be illustrated by the rate equation (S1).

$$\frac{dn}{dt} = -k_1 n - k_2 n^2 - k_3 n^3 \quad (\text{S1})$$

where n is the photoexcited carrier density, k_1 is the first-order recombination constant, k_2 is the second-order recombination constant, and k_3 is the third-order recombination constant.

The TRPL decay curves are derived from an average of TRPL mapping data in an area of 80 μm × 80 μm, which are presented for the control, SIG60 (10 min), and SIG60 (2 min) films in Fig. 2c-e. The TRPL mapping measurements were performed under 470 nm pulsed laser excitation with a high fluence of 32.7 μJ/cm² (photon fluence: 7.74×10¹³ photon/cm²) and a repetition rate of 0.5 MHz in an effective confocal area of 6.11×10⁻⁹ cm². At our fluence level of 32.7 μJ/cm², the PL decay curves in Fig. 2b contain other components as well as trap-assisted nonradiative recombination. In this high fluence case, the PL tail decay interpretation is the most appropriate tool for identifying the first-order recombination lifetime^{7,8}. The first-order recombination lifetime can be extracted by fitting the exponential decay within the PL tail region.

The photoexcited carrier density (n_0) was calculated to be 1.27×10¹⁸ photon/cm³ by the product of the photon fluence and absorption coefficient. At this level of the photoexcited carrier density, the contribution of third-order recombination should be considered⁶. However, the third-order recombination constant under this carrier density is still very small ($k_3 \ll 10^{-30}$ cm⁶/s)⁹ and is only narrowly observed in the initial stage. Thus, we neglected the third-order mechanism in our PL decay analysis.

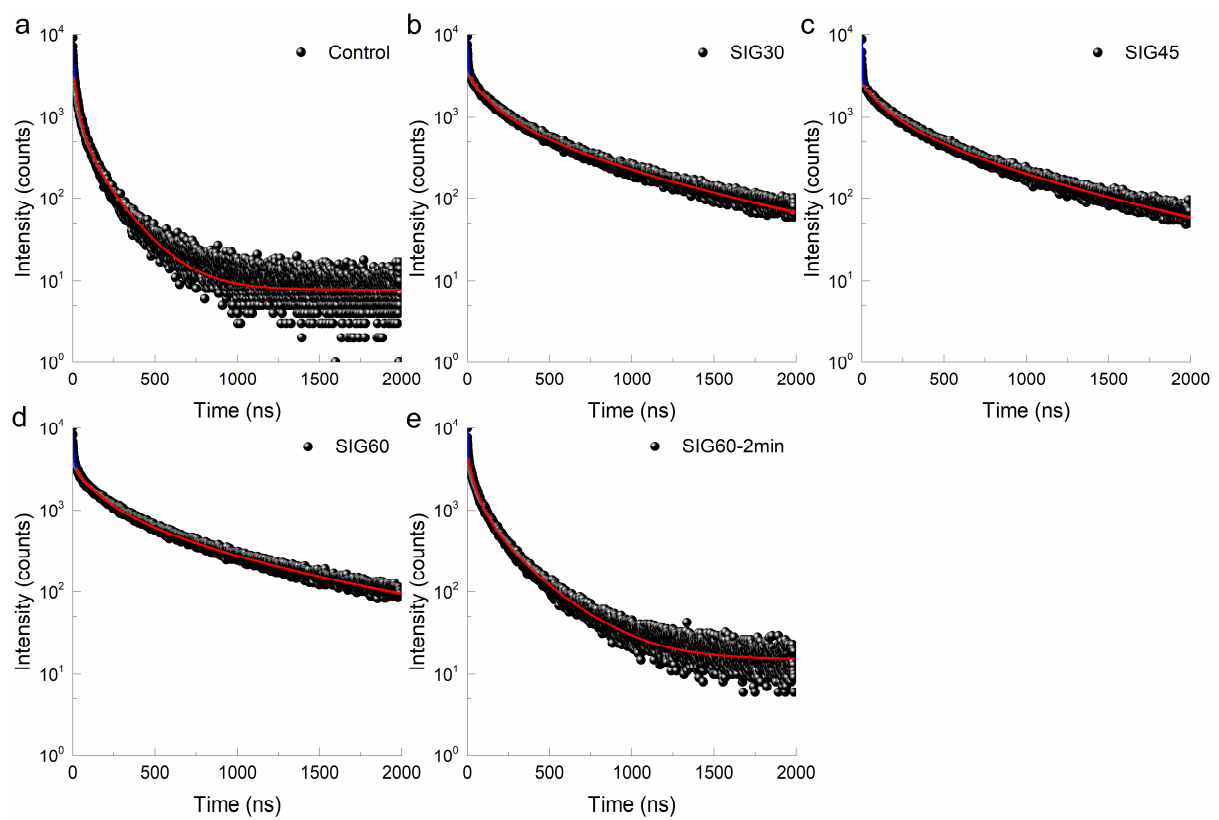
To extract the first-order and second-order recombination constants, we assumed that the PL decay signal is proportional to the photoexcited carrier density as functions of time ($PL(t) \propto n(t)$). The PL decay can be fitted by the below equation (S2)¹⁰.

$$n(t) = \frac{k_1 n_0 e^{-k_1 t}}{k_1 + k_2 n_0 (1 - e^{-k_1 t})} \quad (\text{S2})$$

As described above, the initial time decay (blue solid line), which was ascribed to third-order recombination and observed in all samples, was excluded, and the reliability of the fitting was confirmed through the reduced-Chi square. In Eq. (S2), the first-order lifetime

corresponds to the PL tail decay lifetime¹¹. The parameters acquired for the control and SIG films are summarized in Supplementary Table 3.

As shown in Supplementary Table 3, the second-order recombination constant of all SIG films is clearly reduced compared to the control film. The reduction of the recombination constant is likely caused by the smooth surface of the SIG films¹² or the built-in potential at the 2D/3D heterojunction¹¹.



Supplementary Figure 7. SIG method effect related to the trap-assisted lifetime in TRPL.

a-e, PL decay plots of the control film and SIG films. To identify the first-order recombination lifetime, mono-exponential fitting was used to fit the exponential decay within the PL tail region. Refer to Supplementary Note 1 for details.

Supplementary Table 3. Recombination constant fitted from the PL decay for the control and SIG process conditions.

Condition		First-order	Second-order	Reduced Chi-square
	Lifetime (ns)	k_1 (1/s)	k_2 (cm ³ /s)	
Control	202.89	4.93×10^6	3.18×10^{-10}	1.120
SIG30	1052.77	0.95×10^6	5.35×10^{-11}	1.214
SIG45	1005.35	1.00×10^6	4.17×10^{-11}	1.199
SIG60	1114.22	0.90×10^6	4.79×10^{-11}	1.196
SIG60 2 min	267.48	3.74×10^6	2.09×10^{-10}	1.101

Supplementary Note 2

The SIG process shows improvement of first-order recombination ($\tau = 1/k_1$). As a result, the carrier lifetime increases from 0.2 μs to approximately 1.1 μs . According to the formula in ref.¹³, the carrier lifetime informs us about the achievable V_{OC} if we know several factors, such as the bandgap ($E_g \sim 1.55 \text{ eV}$), short-circuit current density ($J_{SC} \sim 24.80 \text{ mA/cm}^2$), active layer thickness ($d \sim 560 \text{ nm}$), and effective density of states of electrons/holes in the conduction and valence bands ($N_{C,V}$)¹⁴.

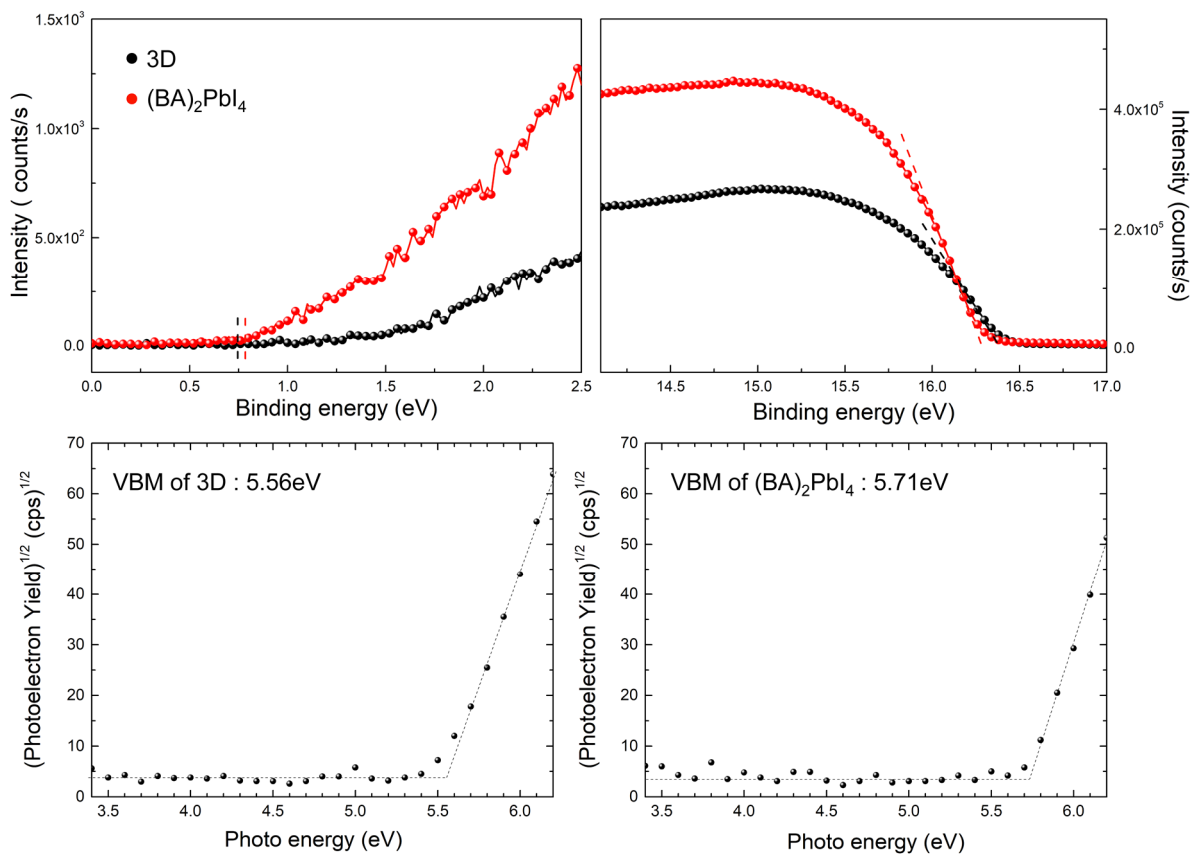
$$eV_{oc} = E_g + k_B T \ln\left(\frac{n_e n_h}{N_c N_V}\right) \quad (\text{S3})$$

where k_B is the Boltzmann constant, T is the Kelvin temperature, and n_e and n_h are the density of electrons and holes in the conduction and valance bands, respectively. Assuming that the carrier generation rate ($G \sim J_{SC}/ed$) is only decreased by the first-order recombination and that the concentrations of electrons and holes are the same, the densities of electrons and holes are approximated by the following equation (S4).

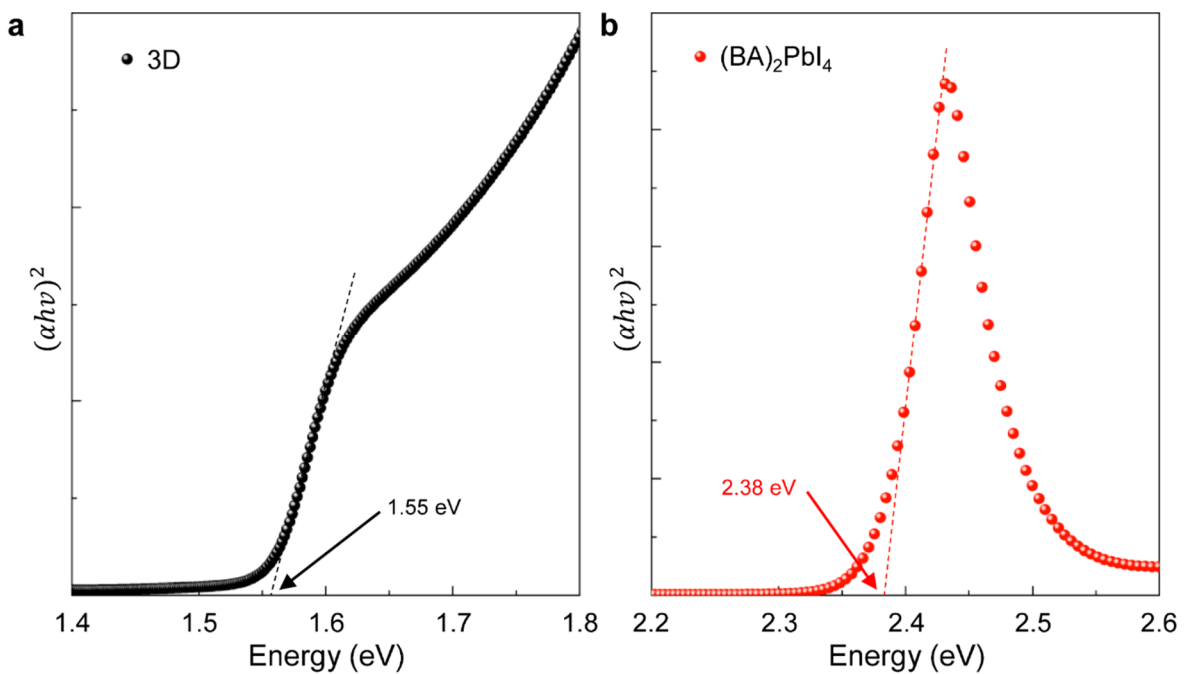
$$n_{e,h} \sim G\tau \quad (\text{S4})$$

Thus, V_{OC} is estimated to 1.16 V by using Eq. (S3) and Eq. (S4) with the 1.1 μs of first-order recombination lifetime obtained from TRPL of SIG perovskite layers (Supplementary Fig. 7 and Supplementary Table 3).

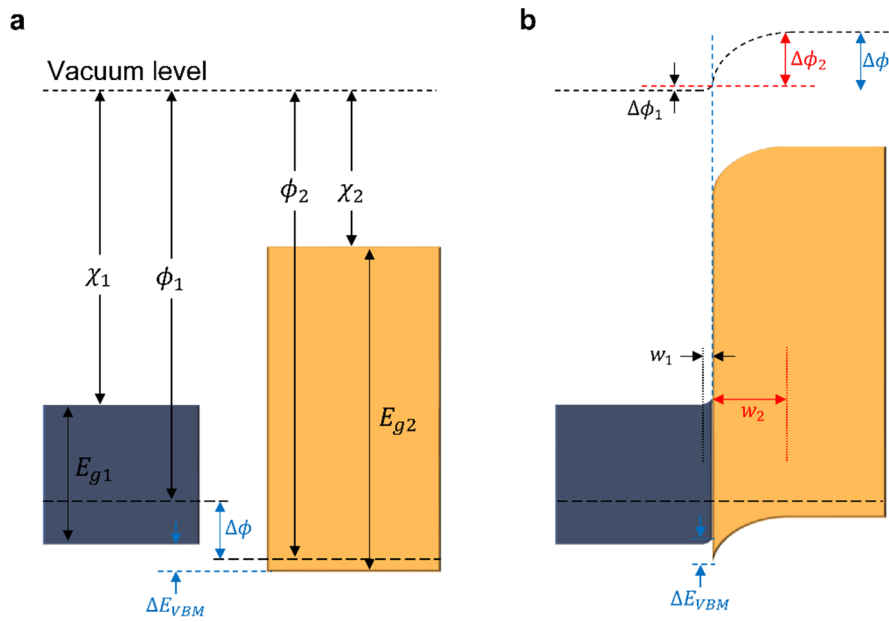
The estimated V_{OC} is much smaller than the theoretical V_{OC} limit (1.278 V) of the photovoltaic device with a bandgap of 1.55 eV because the 1.1 μs is not enough¹⁵. Nevertheless, it is interesting to show higher V_{OC} (1.185 V) in the SIG60 device than the estimated V_{OC} of 1.16 V. In particular, the increase in V_{OC} from 1.117 V to 1.185 V with increasing 2D thickness in spite of a similar recombination lifetime of 1.1 μs level for SIG30, SIG45, and SIG60 perovskite layers in Supplementary Table 3 means that not only the recombination lifetime but also other factor related to the thickness of the 2D layer was involved in V_{OC} of SIG devices.



Supplementary Figure 8. Ultraviolet photoelectron spectroscopy and photoelectron spectroscopy in air of 3D perovskite and $(\text{BA})_2\text{PbI}_4$ films. **a**, Ultraviolet photoelectron spectra of the control 3D film and $(\text{BA})_2\text{PbI}_4$ film. Work functions of each film were determined by the secondary electron onset (right panel), and the valence band maximums of each film was measured by the intercept to zero intensity (position marked by vertical dashed line in left panel). **b-c**, Photoelectron spectroscopy in air of the control 3D film and $(\text{BA})_2\text{PbI}_4$ film. The valence band maximum (VBM) of the 3D film and $(\text{BA})_2\text{PbI}_4$ film was measured to be 5.56 eV and 5.71 eV, respectively, from the threshold photon energy in the linear region.



Supplementary Figure 9. Optical bandgap of the control 3D and $(\text{BA})_2\text{PbI}_4$ films. a-b,
 Tauc plots for bandgap estimation of the control film and $(\text{BA})_2\text{PbI}_4$ film. To identify the optical bandgap of each film, a linear fitting was used for the linear region of the Tauc plot. From the x-axis intercept of the linear function, the optical bandgap of 3D perovskite and $(\text{BA})_2\text{PbI}_4$ films was estimated to 1.55 eV and 2.38 eV, respectively.



Supplementary Figure 10. Energy band profile of the *p*-*p* isotype heterojunction corresponding to the SIG film. **a**, Energy band diagram of each semiconductor before the *p*-*p* isotype heterojunction is formed. **b**, Equilibrium energy band diagram after the *p*-*p* isotype heterojunction is formed.

Supplementary Note 3

According to the Anderson model, the heterojunction between narrow-gap and wide-gap materials is classified by each semiconducting character into the following four cases¹⁶: (1) *n-n*, (2) *n-p*, (3) *p-n*, and (4) *p-p* heterojunctions. In the *p-p* isotype heterojunction, the relation between the electron affinity (χ), bandgap (E_g), and work function (ϕ) of each semiconductor additionally classifies the heterojunction into four cases¹⁷: if E_{g1} has larger bandgap E_{g2} ($E_{g1} < E_{g2}$),

Case I: $\chi_1 > \chi_2$, $\phi_1 < \phi_2$, and $\chi_1 + E_{g1} < \chi_2 + E_{g2}$

Case II: $\chi_1 > \chi_2$, $\phi_1 > \phi_2$, and $\chi_1 + E_{g1} < \chi_2 + E_{g2}$

Case III: $\chi_1 > \chi_2$, $\phi_1 > \phi_2$, and $\chi_1 + E_{g1} > \chi_2 + E_{g2} > \chi_1$

Case IV: $\chi_1 < \chi_2$, $\phi_1 < \phi_2$, and $\chi_1 + E_{g1} > \chi_2$

Our 3D:SIG-(BA)₂PbI₄ bilayer film corresponds to **case I** of the *p-p* heterojunction, as shown in Supplementary Fig. 10, $\chi_1 > \chi_2$, $\phi_1 < \phi_2$, and $\chi_1 + E_{g1} < \chi_2 + E_{g2}$. In **case I**,

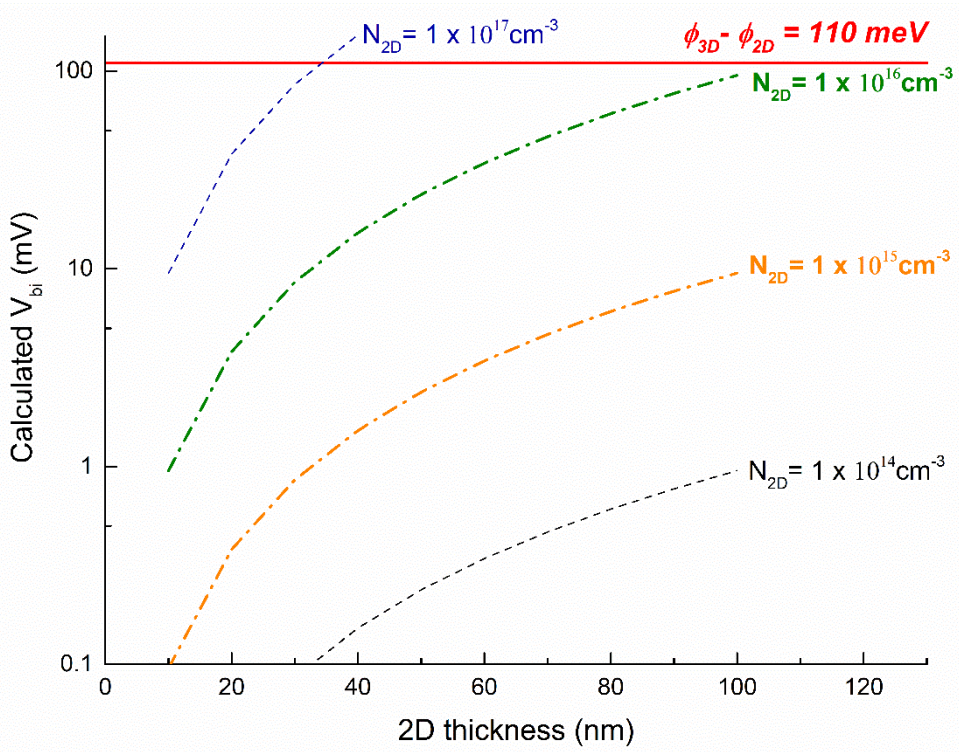
depletion and accumulation regions are formed in the wide-bandgap semiconductor (yellow) and narrow-bandgap semiconductor (grey), respectively¹⁶. The width (w_2) of the depletion region is larger than the accumulation layer width (w_1), and the built-in potential obtained by the heterojunction is mainly dominated by the built-in potential ($\Delta\phi_2$) of the wide-bandgap semiconductor^{16,17}, as shown in Supplementary Fig. 10b. Therefore, the built-in potential formed by the *p-p* isotype heterojunction is as follows.

$$V_{bi} \approx \Delta\phi_2 = \frac{qN_2}{2\varepsilon_2} (w_2)^2 \quad (\text{S5})$$

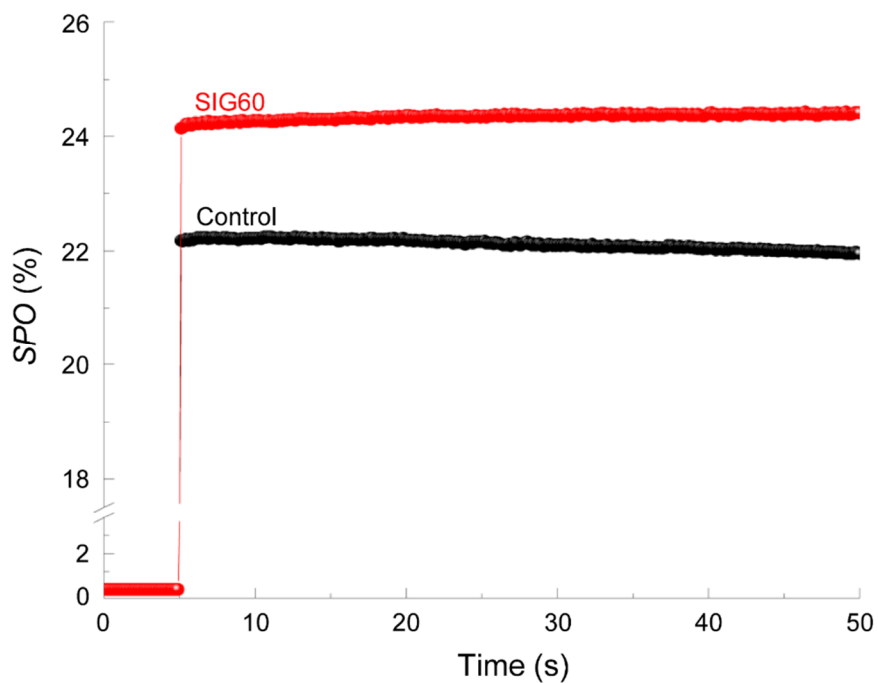
where ε_2 is the relative dielectric constant of the wide-bandgap semiconductor and N_2 is the carrier concentration of the wide-bandgap semiconductor.

For the calculation, ε_{2D} and N_{2D} are needed in Eq. (S5). The N_{2D} of $(\text{BA})_2\text{PbI}_4$ is not yet clear, while the ε_{2D} of $(\text{BA})_2\text{PbI}_4$ was reported to be 9.5 from previous research¹⁸. Therefore, we estimated N_{2D} to be approximately $10^{15}\sim10^{16} \text{ cm}^{-3}$ based on the reported conductivity of polycrystalline $(\text{BA})_2\text{PbI}_4$ and the mobility of single crystalline $(\text{BA})_2\text{PbI}_4$ ^{19,20}.

According to Eq. (S5), the thickness of $(\text{BA})_2\text{PbI}_4$ should be 108 ~304 nm to form the V_{bi} as much as the work function difference (~ 0.11 eV) between 3D and $(\text{BA})_2\text{PbI}_4$ in the *p-p* heterojunction considering of N_{2D} range ($10^{15} \sim 10^{16} \text{ cm}^{-3}$). Thus, in the study where the maximum thickness of $(\text{BA})_2\text{PbI}_4$ is less than 100 nm, the formed built-in potential at the *p-p* isotype heterojunction between the 3D material and $(\text{BA})_2\text{PbI}_4$ can be estimated using Eq. (S5) by replacing w_2 with the thickness of the $(\text{BA})_2\text{PbI}_4$ layer. The calculated results for different carrier concentrations (N_{2D}) of the $(\text{BA})_2\text{PbI}_4$ layer are presented in Supplementary Fig. 11.



Supplementary Figure 11. Calculated built-in potential at the 3D/ $(BA)_2PbI_4$ heterojunction. The built-in potentials were calculated for different carrier concentrations (N_{2D}) of $(BA)_2PbI_4$. The solid red line shows the value for work function difference of 3D and $(BA)_2PbI_4$.



Supplementary Figure 12. Stabilized power output (SPO) of the control and SIG60 devices. Unencapsulated control and SIG60 devices were measured for 50 s at a fixed voltage under simulated AM 1.5G (100 mW/cm^2) in air. The fixed voltage was set to the maximum power point identified from the J-V curve (control: 0.98 V, SIG: 1.01 V).



Technology and Application Center
PV Lab

Calibration Cert. # 2893.01

Newport Calibration Cert. # 2214

DUT S/N: 7212614 D3-P2

Newport Calibration #: 2214

Manufacturer: Korea University/Seoul National University

Material (single junction): Perovskite Solar Cell

Measurement Date: 25-Oct-2019

Temperature Sensor: TC-K, DUT Temperature: 24.95 ± 0.74 °C

Environmental conditions at the time of calibration: Temperature: 24 ± 3 °C, Humidity: 30 ± 20 %

The above DUT has been tested using the following methods to meet the ISO 17025 Standard by the PV Lab at Newport Corporation. Quoted uncertainties are expanded using a coverage factor of $k = 2$ and expressed with an approximately 95% level of confidence. Measurement of total irradiance is traceable to the World Radiometric Reference (WRR) and all other measurements and uncertainties are traceable to NIST and the International System of Units (SI). The performance parameters reported in this certificate apply only at the time of the test, and do not imply future performance.

*Active area as defined by thin metal aperture mask.

[†]Reported performance parameters were measured under a 10 point IV sweep configuration wherein the bias voltage (current for Voc determination) is held constant until the measured current (voltage for Voc) is determined to be unchanging. This is intended to represent the quasi-steady-state performance of the device. Total IV measurement time under these conditions was approximately 8 minutes.

Efficiency [%]	24.35^{\dagger} \pm 0.78	V _{oc} [V]	1.1728 \pm 0.0090	I _{sc} [A]	0.002337 \pm 0.000049
P _{max} [mW]	2.291 \pm 0.068	V _{max} [V]	1.028 \pm 0.015	I _{max} [A]	0.002229 \pm 0.000051
FF [%]	83.6 \pm 1.6	Area [cm ²]	0.09410 [*] \pm 0.00070	M	0.986 \pm 0.015

Methods:

I-V: ASTM E948-16 *Standard Test Method for Electrical Performance of Photovoltaic Cells Using Reference Cells Under Simulated Sunlight*

QE: ASTM E1021-15 *Standard Test Method for Spectral Responsivity Measurements of Photovoltaic Devices*

Standard Reporting Conditions:

Spectrum: AM1.5-G (ASTM G173-03/IEC 60904-3 ed. 2)
 1000.0 W/m^2 at 25.0°C

Secondary Reference Cell:

Device S/N: 10510-0054 KG1
Device Material: mono-Si
Window Material: KG1
Certification: National Renewable Energy Laboratory
A2LA accreditation certificate # 2236.01
ISO Tracking #: 2009

Certified short circuit current (I_{sc}) under standard reporting conditions (SRC): 57.12 mA

Calibration due date: 26-Sep-21

Solar Simulator:

Spectrum: Newport Corporation filename *Sol3A_Spectroradiometer_Scan_0210.xls*
Total irradiance: 1000 W/m^2 based on I_{sc} of the above Secondary Reference Cell

Quantum Efficiency for DUT:

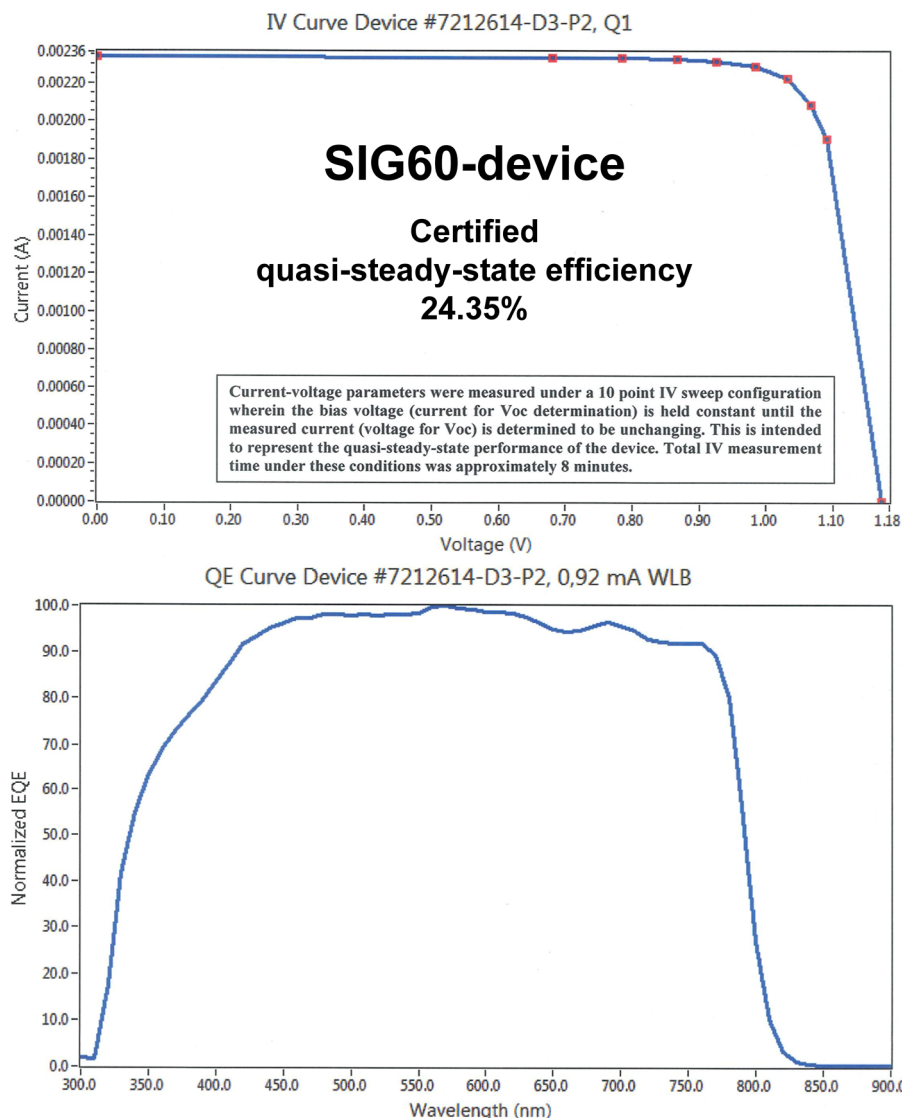
Newport Corporation filename *QE_7212614-D3-P2_0.92_mA_WLB.log*
Spectral mismatch correction factor: M = 0.986 ± 0.015

DUT Calibration Procedures:

Newport Corporation document W11 (EQE).docx
Newport Corporation document Area Measurement W12 (Area).docx
Newport Corporation document W13 (IV.Sweep).docx

Cal Cert V1.8	Issue Date: Nov 01, 2019	Page 2 of 2
Reviewed and Approved by: Geoffrey Wicks (Geoffrey.Wicks@Newport.com)		

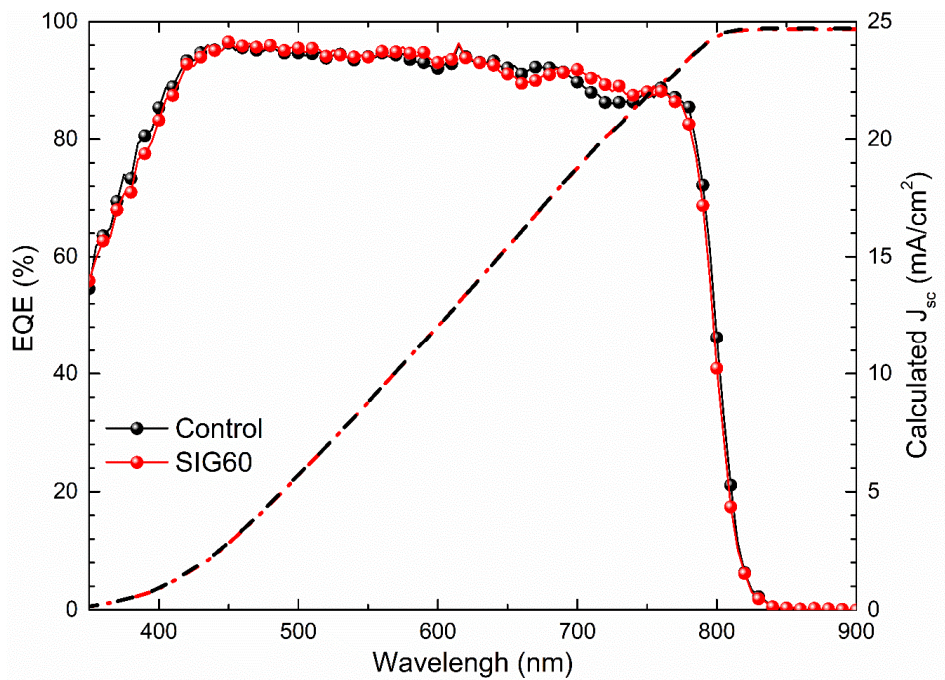
This certificate to be reproduced in part only with written permission from the Newport PV Laboratory



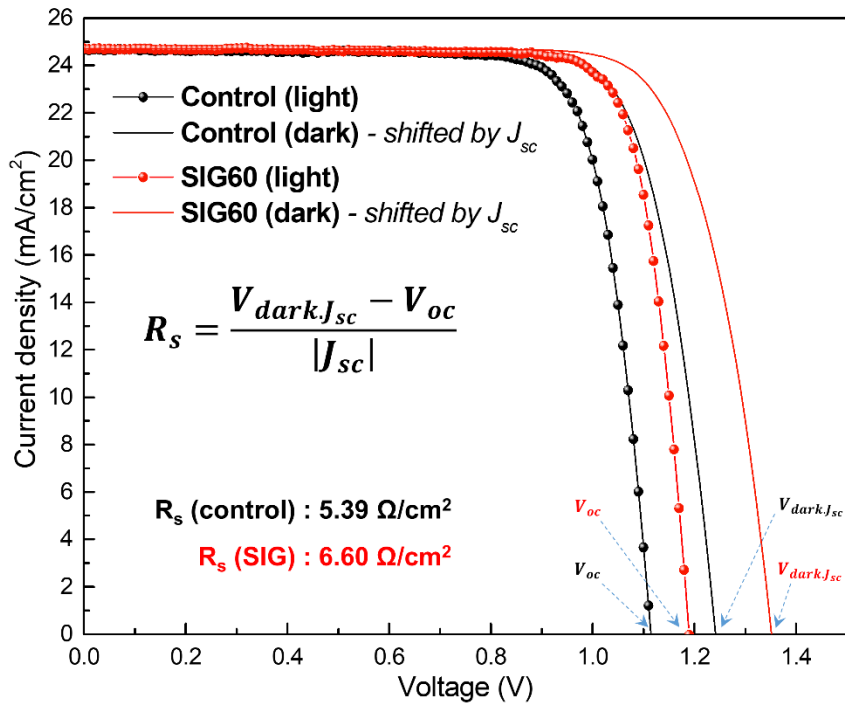
Supplementary Figure 13. Certificate of photovoltaic performance obtained for the SIG device. Newport Co. (USA) summarized the photovoltaic parameters of the SIG60 device (0.094 cm^2) in the certificate.

Supplementary Table 4. Summary of the photovoltaic parameters of devices according to the processing temperature. All parameters were obtained from current density-voltage (J-V) curves measured under 1 sun illumination. Average parameters are displayed as the average value and standard deviation. For each device type, the average parameters were obtained from the arithmetic mean of eight devices.

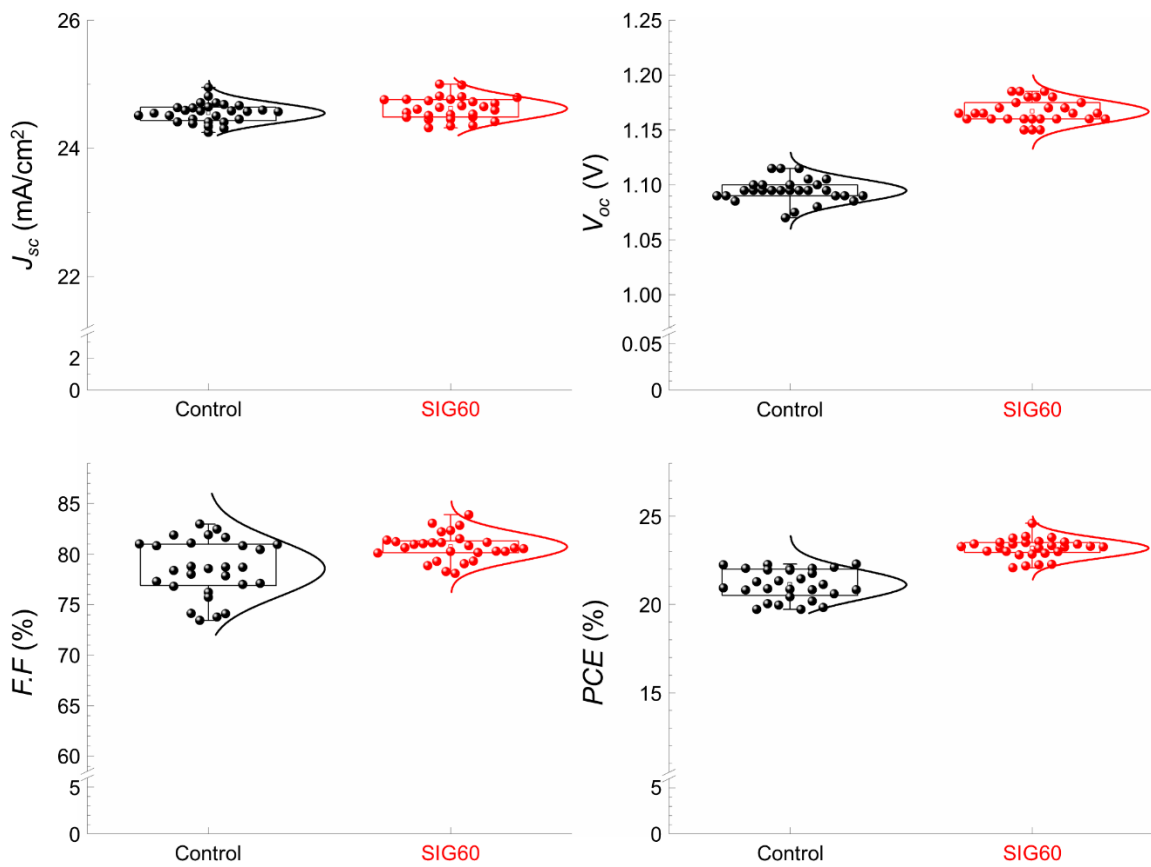
	Device type	J_{SC} (mA/cm ²)	V_{OC} (V)	FF (%)	η (%)
Control	Average	24.56 ± 0.13	1.094 ± 0.005	81.73 ± 0.73	21.95 ± 0.24
	Champion	24.60	1.098	82.95	22.39
SIG30	Average	24.61 ± 0.07	1.118 ± 0.002	81.96 ± 0.39	22.55 ± 0.11
	Champion	24.75	1.117	82.30	22.75
SIG45	Average	24.57 ± 0.17	1.140 ± 0.010	81.57 ± 2.00	22.85 ± 0.63
	Champion	24.68	1.145	84.09	23.76
SIG60	Average	24.64 ± 0.12	1.169 ± 0.011	82.11 ± 1.07	23.67 ± 0.41
	Champion	24.70	1.185	83.90	24.59



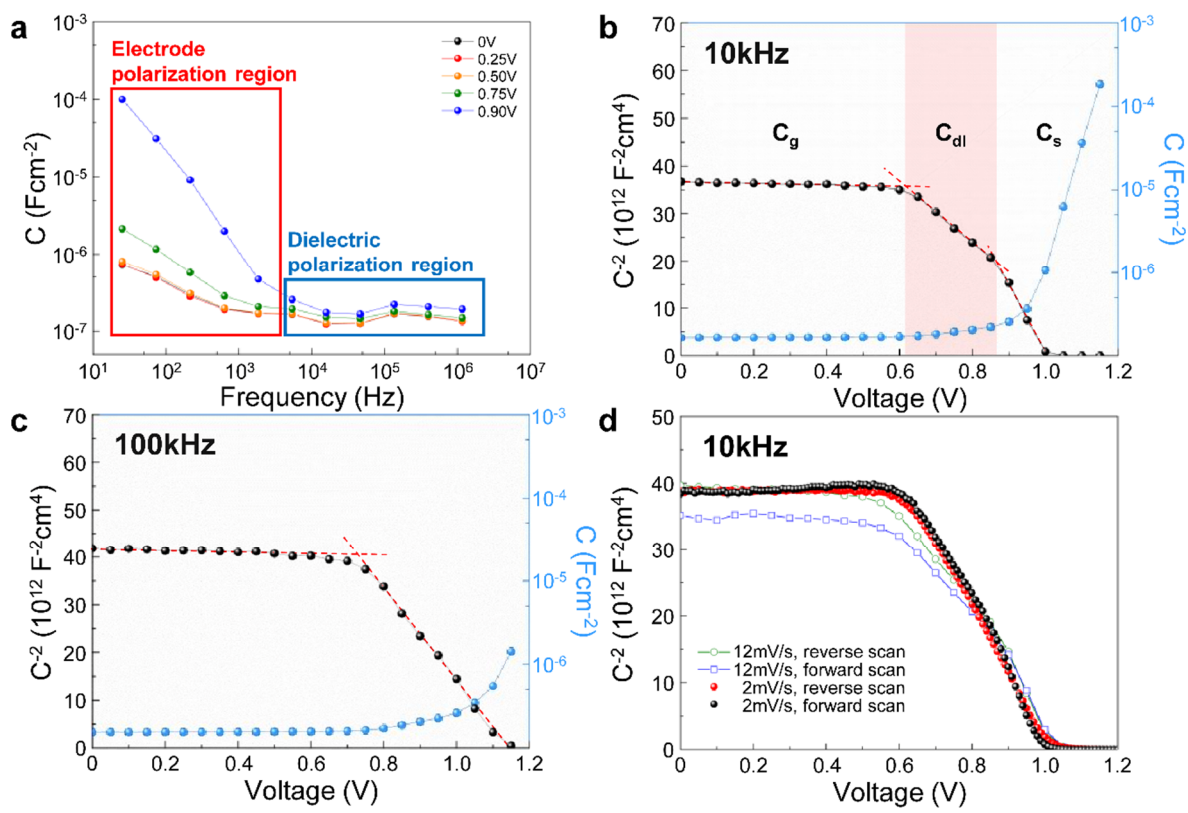
Supplementary Figure 14. External quantum efficiency and calculated short-circuit current density of control and SIG60 devices. EQE spectrum as a function of monochromatic wavelength for the control and SIG60 devices.



Supplementary Figure 15. Series resistance of control and SIG devices. Series resistances were calculated from the J-V curves. Series resistance of the control and SIG devices measured under 1 sun illumination and in the dark. The dark J-V curves are parallel-shifted by the short-circuit current density²¹.



Supplementary Figure 16. Statistical data of the short-circuit current density (J_{sc}), open-circuit voltage (V_{oc}), fill factor (FF) and power conversion efficiency (PCE) for both control and SIG60 devices. All parameters were obtained from 28 cells for both control and SIG60 devices. Each box represents the first quartile to third quartile of data, and the upper and lower points of the error bars show the minimum and maximum values. All performances were detected using a shadow mask of 0.094 cm^2 at room temperature in air.



Supplementary Figure 17. Capacitance-frequency spectrum, capacitance-voltage curve, and Mott-Schottky plot. **a.** Capacitance-frequency spectrum of our control device (FTO/SnO₂/3D/Spiro-OMeTAD/Au) at a DC forward bias in the dark. **b-c.** MS plot and capacitance-voltage curve of the control device at 10 kHz and 100 kHz in the dielectric polarization region. The red dashed line is a guideline to show a distinct capacitance mechanism region in each MS plot. C_g , C_{dl} , and C_s indicate geometrical capacitance, depletion layer capacitance, and electrode polarization capacitance, respectively. **d.** Scan rate and direction effect on the MS plot at 10 kHz.

Supplementary Note 4

The analysis of the Mott-Schottky plots for perovskite solar cells is reported in ref.²². To identify a reliable built-in potential, MS plot and capacitance-voltage curves of PSCs have to show three regions: electrode polarization capacitance dominant region C_s ; depletion layer capacitance dominant region C_{dl} ; and geometrical capacitance dominant region C_g . The following steps must be considered in order to accurately measure the MS plot: (Step 1) identification within the capacitance spectra of the frequency range, (Step 2) selection of a proper measuring frequency within the central plateau of the capacitance spectra, (Step 3) identification of the voltage region dominated by the depletion layer capacitance C_{dl} , and (Step 4) verification of the sensitivity of MS analysis to the scan direction and rate.

According to the above steps, we divided the MS plot measurement into four stages to obtain proper information about the newly formed built-in potential at the 2D/3D junction for full cell devices (FTO/SnO₂/3D:(SIG-2D)/Spiro-OMeTAD/Au).

Step 1) Identification within the capacitance spectra of the frequency range.

To identify the dielectric polarization region (the plateau region of the capacitance spectra) containing the additional contribution of the depletion layer capacitance C_{dl} , the capacitance was measured as a function of frequency from 10¹ Hz to 10⁶ Hz for the control device, as shown in Supplementary Fig. 17a. With several electric biases applied, we found that the section below approximately 5 kHz is the electrode polarization region where the capacitance exponentially grows²³. In contrast, the trend of the capacitance with frequency changes into a plateau for a frequency above 5 kHz, which means that the capacitive mechanisms much more strongly depend on the dielectric polarization. From the capacitance spectra, we can identify two regions of electrode polarization and dielectric polarization for our PSCs.

Step 2) Selection of a proper measuring frequency within the central plateau of the capacitance spectra

In Supplementary Fig. 17a, we can select the proper frequency region from 5×10³ Hz to 10⁶ Hz for the dielectric polarization region to measure the built-in potential of PSCs, which is affected by the depletion layer²². However, not all frequencies allow for the contribution of

the depletion layer capacitance C_{dl} to appear in the MS plot. Therefore, we selected a proper measuring frequency in the next step.

Step 3) Identification of the voltage region dominated by the depletion layer capacitance C_{dl}

To confirm the contribution of the depletion layer capacitance C_{dl} , capacitance-voltage measurements were carried out in the dielectric polarization region. All measurements were performed in the forward direction at 2 mV/s. We determined that the contribution of C_{dl} clearly appears in the MS plot at 10 kHz in Supplementary Fig. 17b, while the contribution of C_{dl} is not presented at 100 kHz in Supplementary Fig. 17c. Because three voltage regions should be differentiated for correct MS analysis, as shown in Supplementary Fig. 17b, we can select the proper frequency of 10 kHz.

Step 4) Verification of the sensitivity of MS analysis to the scan direction and rate.

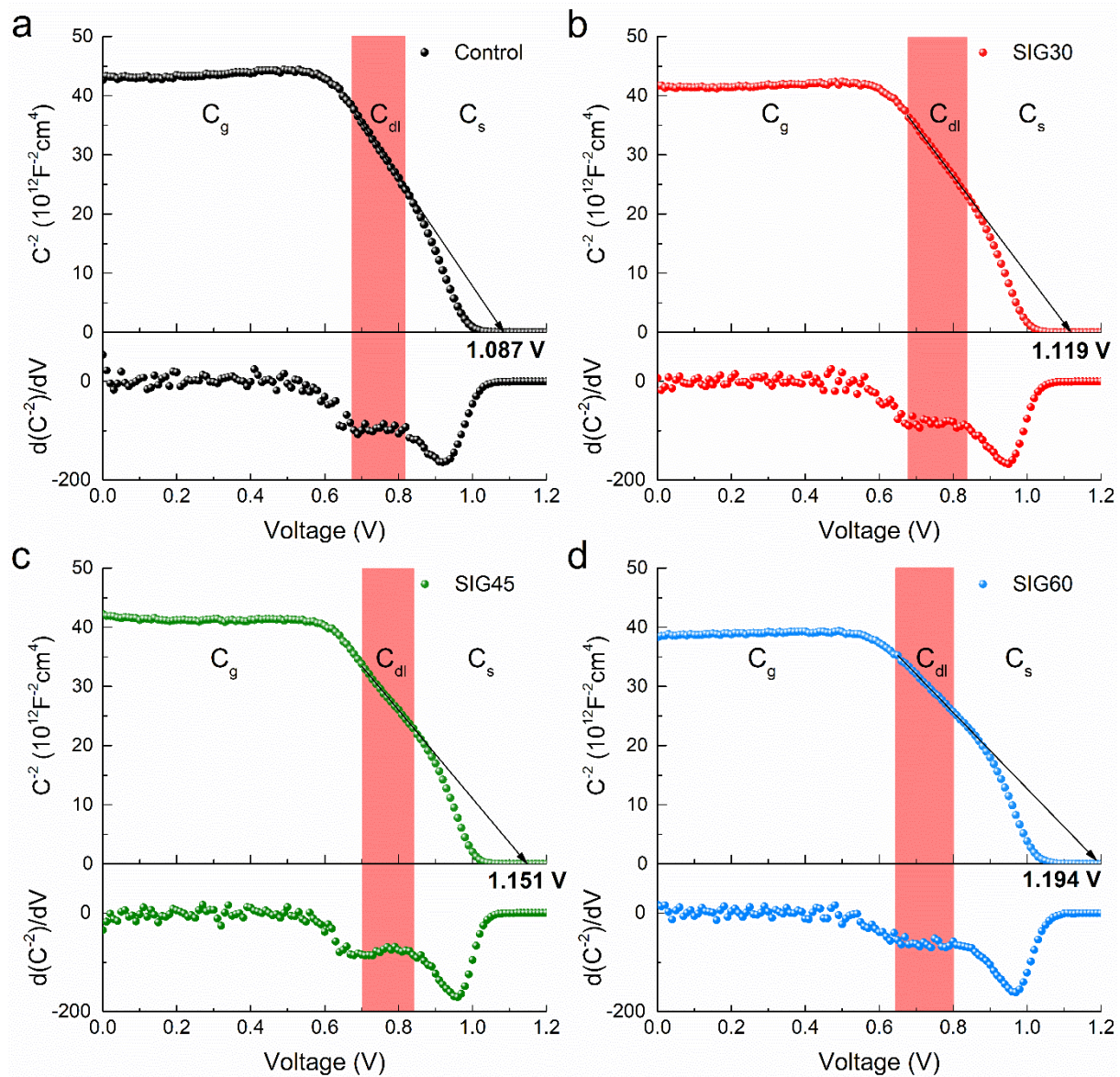
Finally, to verify the measurement conditions of the scan direction and rate for the obtained MS plot, we investigated the behaviour of the MS plot with varying scan direction and rate at the fixed frequency of 10 kHz. Supplementary Fig. 17d shows MS plots obtained under different scan directions and rates at 10 kHz. The slow scan rate (2 mV/s) shows negligible hysteresis, while the fast scan rate (12 mV/s) shows apparent hysteresis in the MS plot. Therefore, we confirmed that the measurement conditions of the scan direction (forward), scan rate (2 mV/s), and frequency (10 kHz) are proper for analysing the MS plot for our PSCs.

Mott-Schottky plots for control and SIG devices

Reliable MS plots were obtained for control and SIG devices under the selected measurement conditions (2 mV/s, forward scan, and 10 kHz) through the above steps. The MS plots are presented in Supplementary Fig. 18. All MS plots clearly show the region of C_{dl} . Therefore, we can obtain the built-in potentials (V_{bi}) for all devices by the linear fitting derived from Eq. (S6).

$$C_{dl} = \sqrt{\frac{q\epsilon\epsilon_0 N}{2(V_{bi}-V)}} \quad (S6)$$

where q is the elementary charge, ϵ_0 is the vacuum permittivity, ϵ is the relative dielectric constant of the perovskite material, N is the carrier density, and V_{bi} is the built-in potential. The obtained V_{bi} values along with V_{OC} values for devices are summarized in Supplementary Table 5.

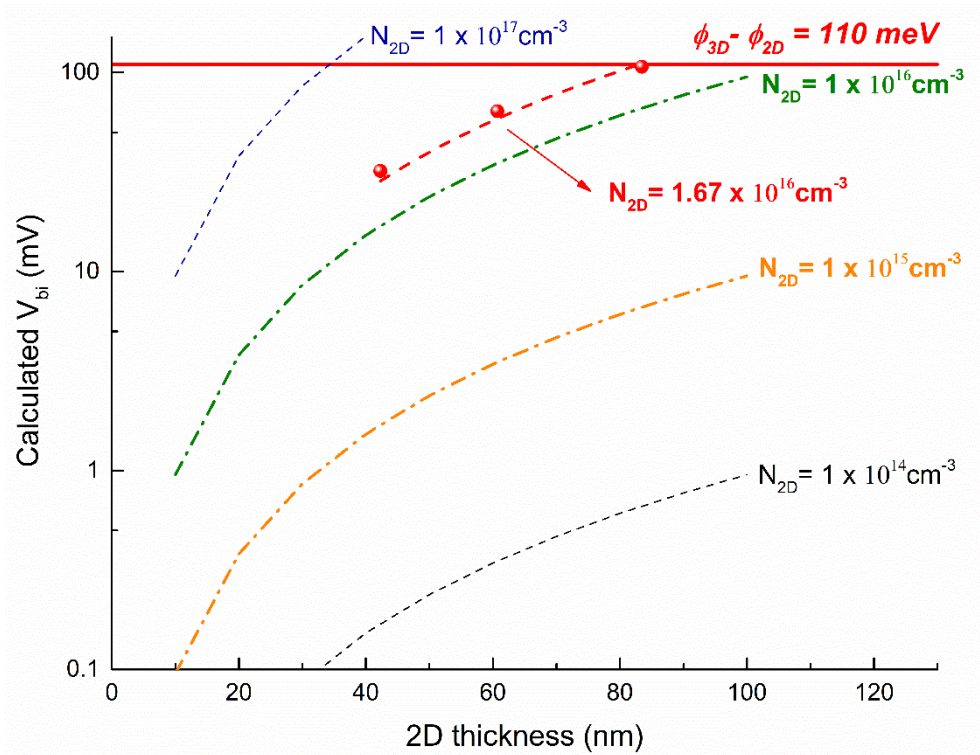


Supplementary Figure 18. Mott-Schottky plot of control and SIG devices. The MS plot measurement conditions were determined to be a 10 kHz frequency, a forward scan direction, and a 2 mV/s scan rate based on Supplementary Fig. 17. To extract the built-in potential from each MS plot, a linear function was fitted using a derivative of C^{-2} .

Supplementary Table 5. Change in the built-in potential and open-circuit voltage in SIG devices. The measured built-in potential (V_{bi}) was obtained from the MS plots in Supplementary Fig. 18. The open-circuit voltage (V_{oc}) was obtained from photovoltaic parameters in Supplementary Table 4. Calculated built-in potential (V_{bi}) was obtained using Eq. (S5) in Supplementary Fig. 10.

Condition	2D thickness (nm)	First-order lifetime (μs)	V_{bi} of MS plot (mV)		V_{oc} of each device (mV)		V_{bi} from Eq. (S5) (mV)
			V_{bi}	ΔV_{bi}	V_{oc}	ΔV_{oc}	
Control		0.20	1087	-	1098	-	-
SIG30	42.30 ± 1.18	1.05	1119	32	1117	19	28.48 ± 1.59
SIG45	60.70 ± 1.09	1.00	1151	64	1145	47	58.62 ± 2.11
SIG60	83.45 ± 1.45	1.11	1194	107	1185	87	110.80 ± 3.84

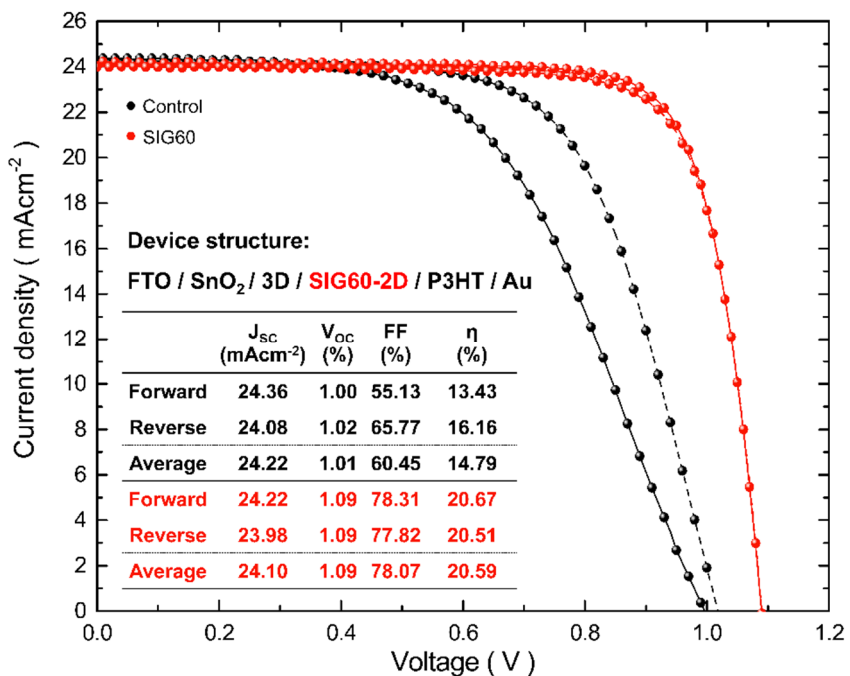
$$N_{2D} = 1.67 \times 10^{16} \text{ cm}^{-3}$$



Supplementary Figure 19. Estimated carrier concentration of SIG-2D films. The carrier concentration ($N_{2D} = 1.67 \times 10^{16} \text{ cm}^{-3}$) was calculated by the built-in potential from the MS plot and the thickness of the SIG films through Eq. (S5).

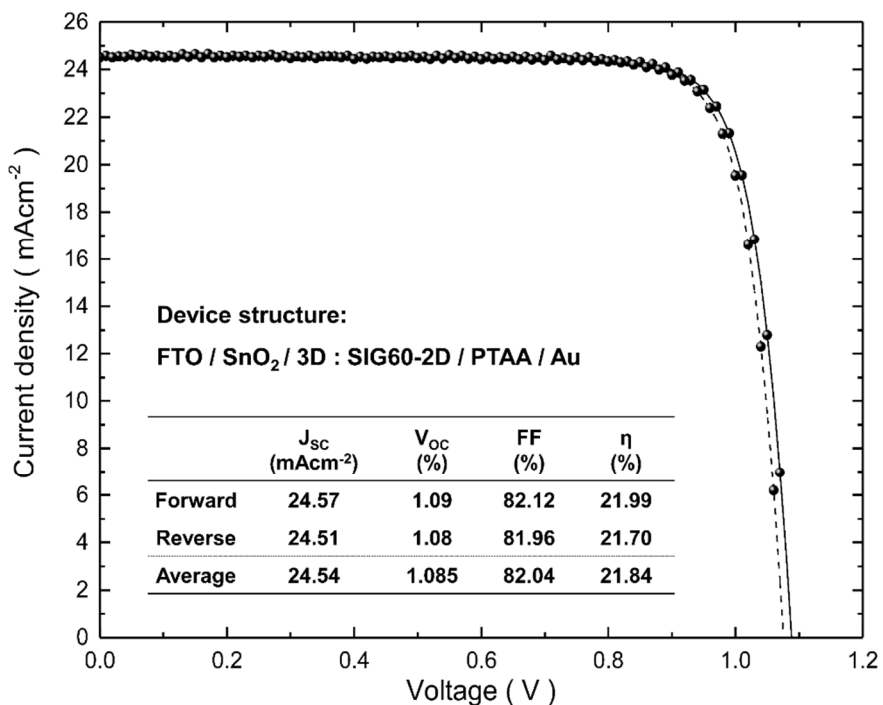
Supplementary Table 6. Summary of the photovoltaic parameters of devices according to the type of hole transfer layer. The open-circuit voltage was improved in all devices using Spiro-OMeTAD, PTAA, and P3HT, and the efficiency of P3HT showed the most dramatic change. The displayed efficiency and each parameter are the average values for forward and reverse scans obtained from the J-V curves.

Hole-transporting material	Structure	J_{sc} (mA/cm ²)	V_{oc} (V)	FF (%)	η (%)
Spiro-OMeTAD	Control	24.60	1.095	82.95	22.39
	SIG60	24.69	1.185	83.95	24.59
PTAA	Control	24.52	1.065	81.78	21.36
	SIG60	24.61	1.105	81.90	22.27
P3HT	Control	24.00	0.970	51.14	11.92
	SIG60	24.17	1.123	75.60	20.52

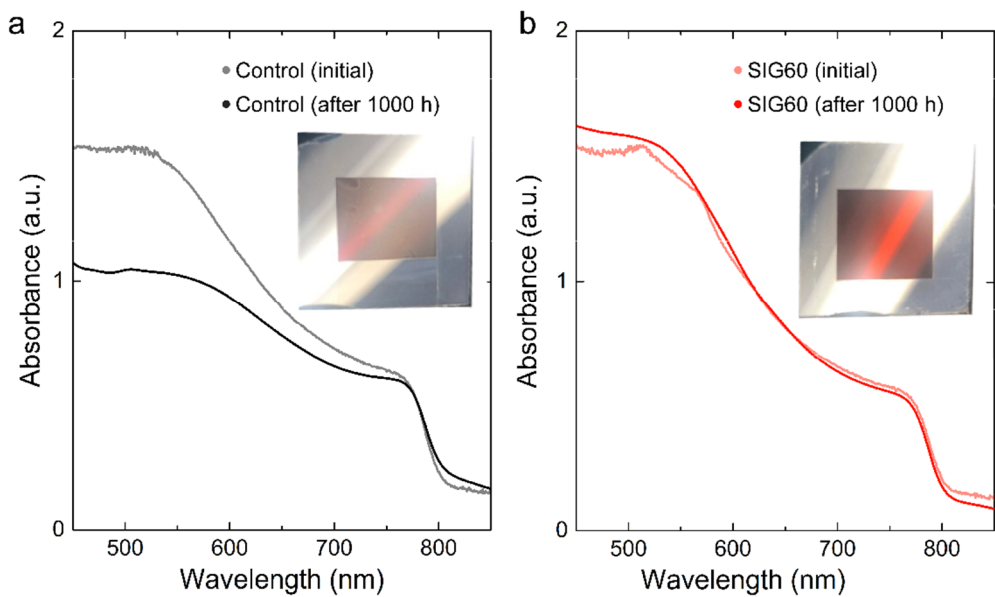


Supplementary Figure 20. Initial current density-voltage (J-V) curves and PV parameters of the control and SIG devices with undoped P3HT as a hole transport layer.

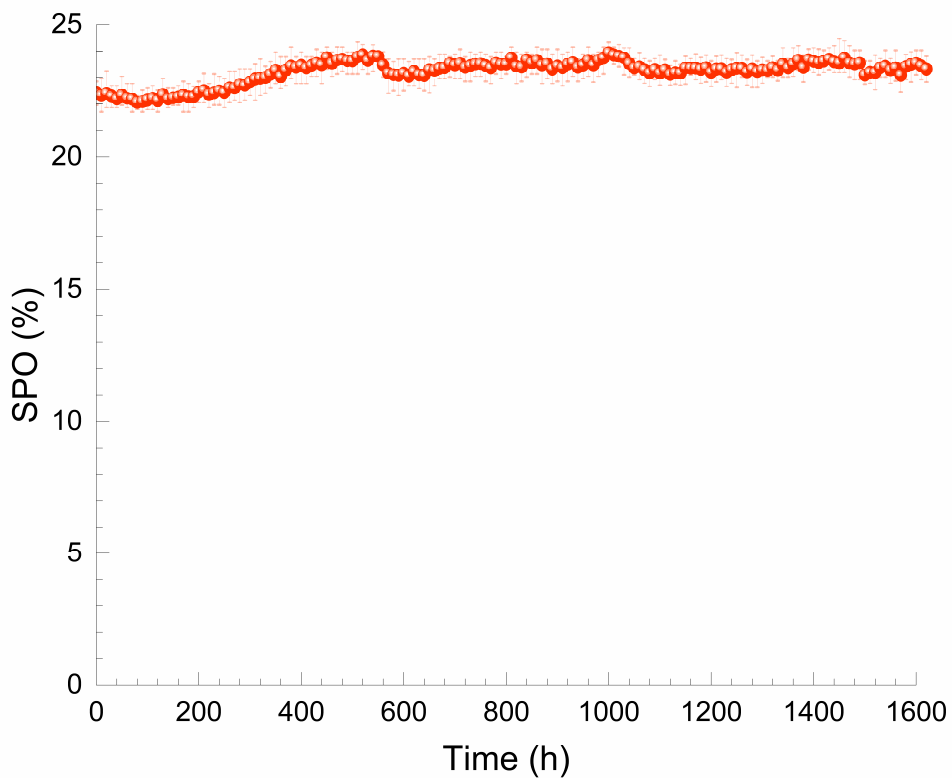
The control and SIG devices were fabricated in the same structure (FTO/SnO₂/3D:SIG-2D/undoped P3HT/Au) except for SIG-processed (BA)₂PbI₄. Solid and dashed lines represent curve measured through the forward scan and reverse scan directions, respectively. These devices were used for humidity stability tests under 85% relative humidity at 25°C.



Supplementary Figure 21. Initial voltage-current density (J-V) curves and PV parameters of the control and SIG devices with doped PTAA as a hole transport layer. Solid and dashed lines show curve measured through the forward scan and reverse scan directions, respectively. For encapsulation, the SIG device and glass cover were attached by UV-induced resin in a N₂ glove box. The stability test under 85% relative humidity at 85°C in the dark was carried out with a device of the same structure.



Supplementary Figure 22. Humidity stability of control and SIG60 films on FTO/SnO₂ substrates. **a-b,** Stability tests were carried out with the control (a; FTO/SnO₂/3D) and SIG60 (b; FTO/SnO₂/3D:SIG60-2D) films under 85% relative humidity at 25°C in the dark. The pictures in panels are the control film and the SIG60 film after 1000 h under the abovementioned condition, respectively. Fresh control and SIG60 films were measured just before exposure to 85% relative humidity at 25°C. After 1000 h of exposure under 85% relative humidity at 25°C the films were removed from dark chamber to remeasure the UV-Vis absorption spectrum.



Supplementary Figure 23. Long-term operational stability. SPO of encapsulated SIG60 devices measured for 1620 h at a voltage near the maximum power point under simulated AM 1.5G (100 mW/cm²). The error bars show the maximum and minimum efficiency for each measuring time.

Supplementary References

- (1) Jeon, N. J. *et al.* Compositional engineering of perovskite materials for high-performance solar cells. *Nature* **517**, 476-480 (2015).
- (2) Cao, D. H., Stoumpos, C. C., Farha, O. K., Hupp, J. T. & Kanatzidis, M. G. 2D homologous perovskites as light-absorbing materials for solar cell applications. *Journal of the American Chemical Society* **137**, 7843-7850 (2015).
- (3) Chen, Y. *et al.* Strain engineering and epitaxial stabilization of halide perovskites. *Nature* **577**, 209-215 (2020).
- (4) Jeon, N. J. *et al.* Solvent engineering for high-performance inorganic–organic hybrid perovskite solar cells. *Nature Materials* **13**, 897-903 (2014).
- (5) Lee, J.-W. *et al.* 2D perovskite stabilized phase-pure formamidinium perovskite solar cells. *Nature Communications* **9**, 3021 (2018).
- (6) Richter, J. M. *et al.* Enhancing photoluminescence yields in lead halide perovskites by photon recycling and light out-coupling. *Nature communications* **7**, 1-8 (2016).
- (7) Zhao, B. *et al.* High-efficiency perovskite–polymer bulk heterostructure light-emitting diodes. *Nature Photonics* **12**, 783-789 (2018).
- (8) Stolterfoht, M. *et al.* Visualization and suppression of interfacial recombination for high-efficiency large-area pin perovskite solar cells. *Nature Energy* **3**, 847-854 (2018).
- (9) Gunawan, O. *et al.* Carrier-resolved photo-Hall effect. *Nature* **575**, 151-155 (2019).
- (10) Knight, A. J. *et al.* Electronic traps and phase segregation in lead mixed-halide perovskite. *ACS Energy Letters* **4**, 75-84 (2018).
- (11) Wolford, D. *et al.* Intrinsic recombination and interface characterization in ‘‘surface-free’’GaAs structures. *Journal of Vacuum Science & Technology B: Microelectronics*

and Nanometer Structures Processing, Measurement, and Phenomena **9**, 2369-2376 (1991).

- (12) Buizza, L. R. *et al.* Charge-Carrier Dynamics, Mobilities, and Diffusion Lengths of 2D–3D Hybrid Butylammonium–Cesium–Formamidinium Lead Halide Perovskites. *Advanced Functional Materials* **29**, 1902656 (2019).
- (13) Tress, W. Perovskite solar cells on the way to their radiative efficiency limit—insights into a success story of high open-circuit voltage and low recombination. *Advanced Energy Materials* **7**, 1602358 (2017).
- (14) Karthick, S., Velumani, S. & Bouclé, J. Experimental and SCAPS simulated formamidinium perovskite solar cells: A comparison of device performance. *Solar Energy* **205**, 349-357 (2020).
- (15) Guillemoles, J.-F., Kirchartz, T., Cahen, D. & Rau, U. Guide for the perplexed to the Shockley–Queisser model for solar cells. *Nature Photonics* **13**, 501-505 (2019).
- (16) Lopez, A. & Anderson, R. L. PHOTOCURRENT SPECTRA OF GE-GAAS HETERO-JUNCTIONS. *Solid-State Electronics* **7**, 695-700 (1964).
- (17) Sharma, B. L. & Purohit, R. K. *Semiconductor heterojunctions*. Ch. 2, (Elsevier, 2015).
- (18) Tsai, H. *et al.* High-efficiency two-dimensional Ruddlesden–Popper perovskite solar cells. *Nature* **536**, 312-316 (2016).
- (19) Zhu, X. *et al.* Vapor-fumigation for record efficiency two-dimensional perovskite solar cells with superior stability. *Energy & Environmental Science* **11**, 3349-3357 (2018).
- (20) Wang, K., Wu, C., Yang, D., Jiang, Y. & Priya, S. Quasi-two-dimensional halide perovskite single crystal photodetector. *ACS nano* **12**, 4919-4929 (2018).

- (21) Mette, A. *et al.* Series resistance characterization of industrial silicon solar cells with screen-printed contacts using hotmelt paste. *Progress in photovoltaics: research and applications* **15**, 493-505 (2007).
- (22) Almora, O., Aranda, C., Mas-Marzá, E. & Garcia-Belmonte, G. On Mott-Schottky analysis interpretation of capacitance measurements in organometal perovskite solar cells. *Applied Physics Letters* **109**, 173903 (2016).
- (23) Chen, B. *et al.* Impact of capacitive effect and ion migration on the hysteretic behavior of perovskite solar cells. *The journal of physical chemistry letters* **6**, 4693-4700 (2015).



Intact 2D/3D halide junction perovskite solar cells via solid-phase in-plane growth

Yeoun-Woo Jang^{1,2,5}, Seungmin Lee^{3,5}, Kyung Mun Yeom³, Kiwan Jeong¹, Kwang Choi^{1,3}, Mansoo Choi^{1,2} and Jun Hong Noh^{1,3,4}

The solution process has been employed to obtain Ruddlesden-Popper two-dimensional/three-dimensional (2D/3D) halide perovskite bilayers in perovskite solar cells for improving the efficiency and chemical stability; however, the solution process has limitations in achieving thermal stability and designing a proper local electric field for efficient carrier collection due to the formation of a metastable quasi-2D perovskite. Here we grow a stable and highly crystalline 2D $(C_4H_9NH_3)_2PbI_4$ film on top of a 3D film using a solvent-free solid-phase in-plane growth, which could result in an intact 2D/3D heterojunction. An enhanced built-in potential is achieved at the 2D/3D heterojunction with a thick 2D film, resulting in high photovoltage in the device. The intact 2D/3D heterojunction endow the devices with an open-circuit voltage of 1.185 V and a certified steady-state efficiency of 24.35%. The encapsulated device retained 94% of its initial efficiency after 1,056 h under the damp heat test (85 °C/85% relative humidity) and 98% after 1,620 h under full-sun illumination.

Perovskite solar cells (PSCs) have emerged as a strong candidate for future photovoltaic technology owing to their remarkable power conversion efficiency (PCE), which exceeds 25%, and easy fabrication at low temperatures^{1,2}. However, achieving higher performance with long-term stability for commercial use is still a challenge. The strategy of forming Ruddlesden-Popper 2D perovskite layers on the surface of a 3D light-absorbing perovskite layer has recently drawn attention^{3–7}. This strategy has the advantages of reducing surface defects by surface passivation^{3,4} and forming a 2D/3D heterojunction^{5–7}. However, the formation of unidentified phases and an unintended quasi-2D phase hinders the design of an adequate electric field distribution at the junction^{8,9}. The 2D/3D junction should be carefully designed on the basis of photoelectrical properties such as the bandgap and work function¹⁰. It is also necessary to develop fabrication processes that can ensure an effective and stable junction, considering the competitive long-term stability and production cost of solar cell devices^{11,12}.

The general chemical formula of Ruddlesden-Popper 2D and 3D metal iodide perovskites is $(A^*)_2A_{n-1}Pb_nI_{3n+1}$ and $APbI_3$, respectively, where A^* is a large organic cation with a long carbon chain and A is a small organic cation such as $CH_3NH_3^+$ or $HC(NH_2)_2^+$ (refs. ^{13,14}). The symbol n indicates the number of $[PbI_6]^{4-}$ octahedral monolayers between the organic spacer A^* layers and hereby the phase can be classified into three cases: a 2D perovskite ($n=1$, $(A^*)_2PbI_4$); a quasi-2D perovskite ($1 < n < \infty$, $(A^*)_2A_{n-1}Pb_nI_{3n+1}$); and a 3D perovskite ($n=\infty$, $APbI_3$)¹⁵. The 2D phase with $n=1$ is known to be the most stable as the organic spacers are repeated most often¹⁶. There have been many attempts to fabricate PSCs with high PCE and stability using 2D perovskites, including mixing a 2D precursor with a 3D precursor solution^{17–19} or forming a 2D/3D bilayer via the reaction of a 2D precursor solution on the surface of a 3D layer^{3,5,6}. However, these solution processes thus far inevitably form an unintended quasi-2D phase that negatively affects the PCE and stability¹⁶.

In this study we devised a solid-state in-plane growth (SIG) method for growing a 2D layer on a 3D layer by applying pressure and heat to ensure the intact properties of both layers in the complete device. Although pressure-assisted crystallizations of perovskite layers have also been reported before, they have been carried out in a system that includes a liquid-state precursor^{20–22}. The SIG process successfully avoids the formation of unintended phases and can adjust the thickness of the 2D layer. The controllability of the thickness of the intact 2D layer facilitates device optimization for increasing the built-in potential at the junction. The stable 2D layer entirely formed on a 3D surface can maximize the stability enhancement effect.

SIG process

Figure 1a shows a schematic of the procedure of the SIG process. A solid-state 2D film is stacked on top of a 3D film so that their surfaces are in contact. Heat and pressure are then applied perpendicular to the joint surface to induce a supply of the 2D perovskite from the stacked solid 2D precursor film to the top of the 3D film. Two-dimensional seeds are formed at the initial stage and gradually grow on the 3D film in the in-plane direction, becoming a new 2D film. After a specific process time passes, the original 2D solid precursor is detached and then an intact 2D/3D bilayer is finally formed. The characteristics of the SIG are compared to the conventional solution process in Supplementary Table 1.

For the SIG process, 2D $(BA)_2PbI_4$ and 3D $(FAPbI_3)_{0.95}(MAPbBr_3)_{0.05}$ (where FA is formamidinium and MA is methylammonium) films were prepared on substrates. All of the SIG processes were performed at 60 MPa, except for the experiment examining the influence of pressure. The temperature condition is marked after SIG (for example, SIG30 denotes the SIG process at 30 °C and 60 MPa). Figure 1b–f displays scanning electron microscopy (SEM) plan-view images of the SIG60-processed films as a

¹Global Frontier Center for Multiscale Energy Systems, Seoul National University, Seoul, Republic of Korea. ²Department of Mechanical and Aerospace Engineering, Seoul National University, Seoul, Republic of Korea. ³School of Civil, Environmental and Architectural Engineering, Korea University, Seoul, Republic of Korea. ⁴KU-KIST Green School Graduate School of Energy and Environment, Korea University, Seoul, Republic of Korea. ⁵These authors contributed equally: Yeoun-Woo Jang, Seungmin Lee. e-mail: mchoi@snu.ac.kr; junhnoh@korea.ac.kr

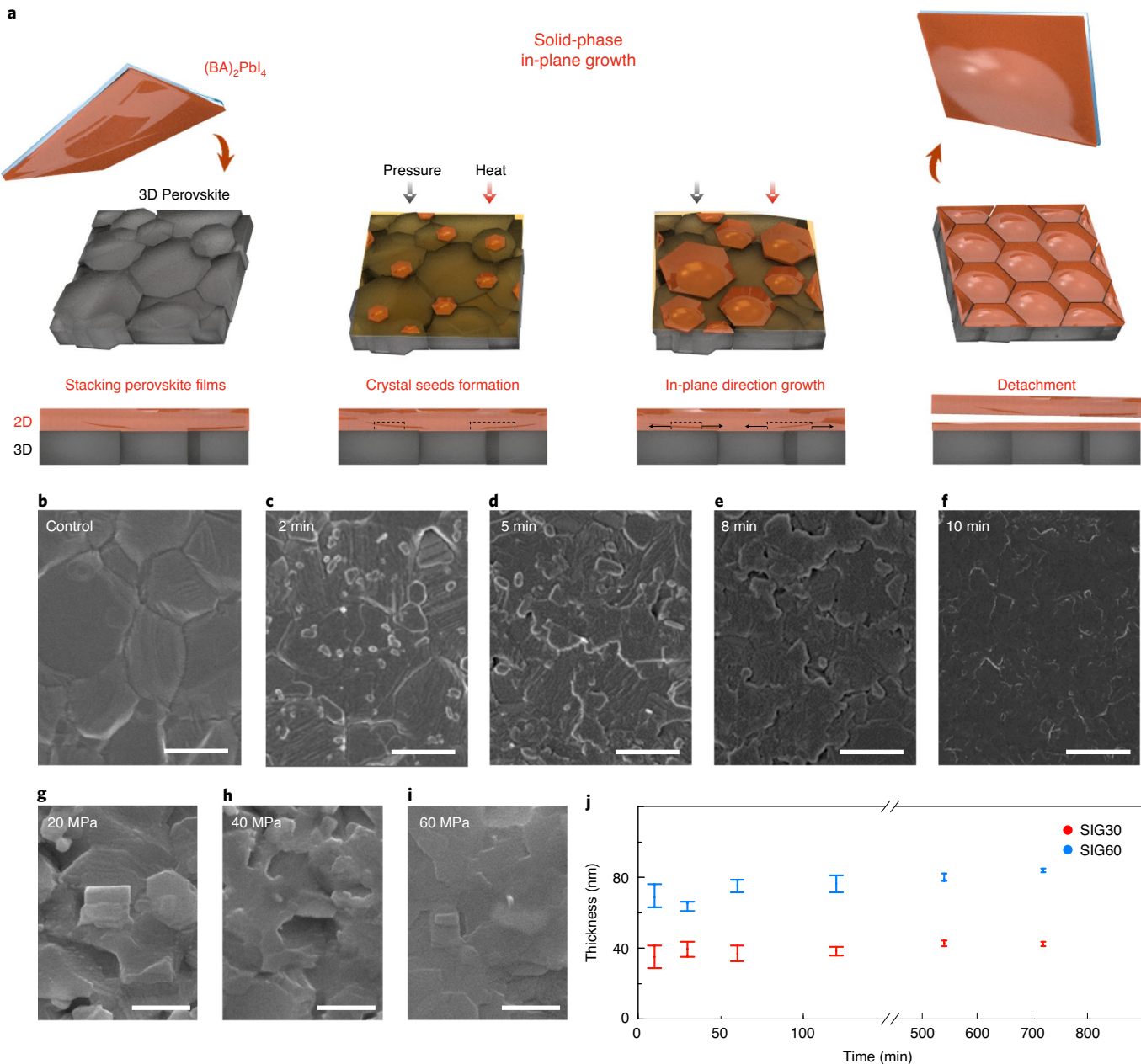


Fig. 1 | SIG process and the effect of pressure, heat and processing time. **a**, Top-view and cross-sectional sketches of the manufacturing of a $(\text{BA})_2\text{PbI}_4$ film on a 3D perovskite substrate via the SIG method. The formation of crystal seeds and the in-plane grain growth are indicated with black dashed lines and black arrows, respectively, in the cross-sectional representation of the perovskite layer. **b–i**, Top surface SEM images of the 3D perovskite (**b**); the 2D/3D perovskite film fabricated under SIG60 conditions after 2 min (**c**), 5 min (**d**), 8 min (**e**) and 10 min (**f**) processing time; and SIG60-processed 2D/3D films after 10 min at 20 MPa (**g**), 40 MPa (**h**) and 60 MPa (**i**). **j**, The thickness distribution of the grown $(\text{BA})_2\text{PbI}_4$ accretion with processing time. Five samples were used in every case to measure the change in thickness over time under SIG30, whereas six samples were used for SIG60. Error bars show the lower and upper thicknesses of $(\text{BA})_2\text{PbI}_4$ at each condition. Scale bars in **b–f** and **g–i** represent 1 μm and 400 nm, respectively.

function of the processing time. The SEM image of a SIG60 2 min case (Fig. 1c) provides a glimpse of the initial state, with tiny seed-like products appearing on the 3D surface. The seeds subsequently became enlarged and gradually filled the 3D surface (Fig. 1c–e). The substance completely covered the 3D surface after 10 min (Fig. 1f). The X-ray diffraction (XRD) results for the same SIG films in Supplementary Fig. 1 support that the planar material observed in the SEM images is $(\text{BA})_2\text{PbI}_4$. Only one new peak appears at 6.4° from 2 min to 10 min, which gradually grows over time. This peak corresponds to the (002) plane of $(\text{BA})_2\text{PbI}_4$ (ref. ²³) and

corresponds with the peak of the original precursor 2D film, revealing that the new 2D film is sourced from the original solid precursor 2D film. Moreover, in Supplementary Fig. 2, the cross-sectional high-resolution transmission electron microscopy (HRTEM) image for the SIG60 10 min film also shows that a crystalline 2D film is successfully formed on top of the 3D film without interfacial interaction.

As seed formation and growth are generally governed by thermodynamic and kinetic factors, we monitored variations in the $(\text{BA})_2\text{PbI}_4$ film formation on the 3D layer with processing pressure,

temperature and time to understand the SIG procedure. The pressure aided intimate contact between the two films and allowed the formation of the initial seeds, which moved from the original 2D film. We observed no occurrence of 2D perovskite accretion on the 3D surface in the absence of pressure (Supplementary Fig. 3). The pressure also promotes the in-plane growth of the 2D layer. Figure 1g–i shows plan-view SEM images for the SIG60 films after 10 min under different pressures. The 2D crystal was still in the process of formation at 20 MPa, whereas it was almost wholly planarized at 60 MPa.

The temperature also strongly influences crystal formation and growth. Figure 1j shows the thicknesses of the 2D films for SIG30 and SIG60 over time. It is notable that thickness increment in the out-of-plane direction hardly occurs over time, even when the processing time is extended to 720 min. This suggests that the seeds grow in the in-plane direction while the height of the initial seeds is maintained over time, probably due to 2D material characteristics. Comparing SIG30 and SIG60, the processing temperature determines the final thickness of the SIG-2D film as the initial height of the seeds is highly dependent on the temperature and their growth has a strong preference for the in-plane direction. As a result, a thicker 2D layer was created at a higher temperature, as shown in Supplementary Fig. 4.

According to classical nucleation theory, the nucleation and growth of a crystal from the initial precursors can be explained by the differences in the Gibbs free energy due to the volume and surface area changes of the newly formed crystal²⁴. In the SIG process, however, a new crystal is not created as a 2D crystal already exists in the stacked original 2D precursor film. We therefore surmise that there would be no free energy changes caused by volume changes, but a surface area change can still occur when the original crystals surrounded by the 2D precursor film change into 2D seeds on the 3D surface. The newly formed surface area of seeds is determined by the balance between the increased free energy and the supplied thermal energy. As a result, the temperature can determine the initial seed height and final thickness of the SIG-2D film (Fig. 1h and Supplementary Fig. 4). We also observed that the seeds did not manage to grow into a 2D film at 20 °C, whereas at 30 °C they succeeded (Supplementary Fig. 5), indicating that sufficient thermal energy is required for the in-plane growth. The anisotropic surface energy of the 2D materials also probably affects the in-plane growth without a thickness increase²⁵.

Formation of an intact 2D/3D multilayer

Figure 2a displays the XRD results for the control 3D film, the original 2D $(\text{BA})_2\text{PbI}_4$ film and the SIG-2D/3D bilayer films formed at different temperatures. All of the SIG films show the (002) peak typical of $(\text{BA})_2\text{PbI}_4$ (at approximately 6.4°) without other peaks for an unknown or quasi-2D phase. The (002) peak grows with the increase in the 2D film thickness, which is determined by the processing temperature. The original 2D film has a very narrow full-width at half-maximum (FWHM) of 0.105° for the (002) peak, and the SIG-2D films on top of the 3D surfaces also show a small value of ~0.167°, including an estimated instrumental broadening of 0.061° at 6.4° (2θ) (Supplementary Table 2). It is notable that the FWHM values for SIG-2D films are considerably smaller than the reported FWHM values of above 0.50° for the (002) peak of the 2D layers obtained by conventional solution processes^{5,17,26,27}. The SIG process enabled the formation of a several-tens-of-nanometres-thick upper layer containing a highly crystalline pure 2D phase on top of a 3D layer. The absence of secondary phases and a clear 2D/3D interface in the HRTEM image (Supplementary Fig. 2) reveal that the SIG process can produce an intact 2D/3D multilayer. We also showed that the SIG process could be valid for pure FAPbI_3 and MAPbI_3 perovskites, thus showing its wide applicability (Supplementary Fig. 6).

Reduction of surface recombination via SIG

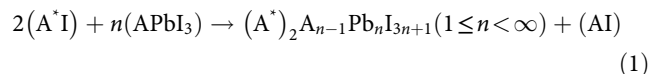
Figure 2b shows the time-resolved photoluminescence (TRPL) decay curves of the control 3D and SIG films. The first-order decay related to trap-assisted non-radiative recombination can be identified by fitting the exponential decay within the photoluminescent tail region^{28,29}. The detail fitting process and results are presented in Supplementary Note 1 and Supplementary Fig. 7, respectively. The obtained recombination constants and lifetimes are summarized in Supplementary Table 3. The SIG process enhances the lifetime of the first-order recombination up to approximately 1.1 μs (from the 0.2 μs control) regardless of the processing temperature. This means that the SIG process reduces trap-assisted non-radiative recombination and that the processing temperature does not influence the carrier lifetime. The reduction of surface defects seems to be independent of the SIG-2D film thickness as the contact area between the 2D and 3D materials is constant.

The change in the average carrier lifetime with processing time is also represented by lifetime mapping in Fig. 2c–e. The blue region with a short lifetime gradually transitions to a green region with a longer lifetime. The partial green region indicates the area that was partially covered by the 2D seeds after 2 min; after 10 min the 2D film had covered all of the area via in-plane growth. The TRPL results reveal that the 2D film successfully passivated the surface of the 3D film via the SIG process. Details on the device performance will be discussed later, but the point to note in the TRPL results is that the improved lifetime of 1.1 μs is insufficient to achieve a high open-circuit voltage ($V_{\text{OC}} \approx 1.185$ V) for the SIG devices in this study according to a previous study on V_{OC} (ref. ³⁰; Supplementary Note 2). Furthermore, the fact that V_{OC} increases as the SIG-2D thickness increases (despite the similar lifetimes of 1.1 μs) has us consider the contributions from other factors to the improvement of V_{OC} .

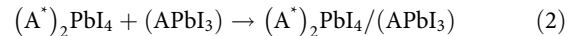
Design of the local electric field at the 2D/3D junction

In addition to surface passivation, the electric field generated by the intact 2D/3D junction can improve the performance of PSCs. The electric field can be designed by controlling the semiconducting properties and thickness of the 2D layer; however, the existing solution process has difficulty forming a clear 2D/3D junction for shaping the optimal electric field⁷. This is because the solution process is based on the reaction between the 2D precursor (A^*I) dissolved in a solvent and the 3D (APbI_3) upper part. The reaction has the problem of producing quasi-2D phases $(\text{A}^*)_2\text{A}_{n-1}\text{Pb}_n\text{I}_{3n+1}$ ($1 < n < \infty$)^{8,31} and not producing a pure 2D $(\text{A}^*)_2\text{PbI}_4$ phase, as the PbI_2 required for reaction with (A^*I) must be supplied by the 3D layer, leaving (AI) according to equation (1).

Existing solution process:



SIG process:



On the other hand, the SIG process produces a definite and highly crystalline 2D ($n=1$) perovskite on the 3D perovskite without any reaction with the 3D surface according to equation (2), which is also confirmed by the above-mentioned XRD and HRTEM studies. The SIG process can not only form an intact 2D/3D junction, but also control the thickness of the 2D layer through the processing temperature or an iteration process; the electric field thus becomes designable.

We conducted the SIG and solution processes twice (iteration process) to assess the potential for electric field design by ensuring an adequate 2D thickness. Figure 3a–c shows the

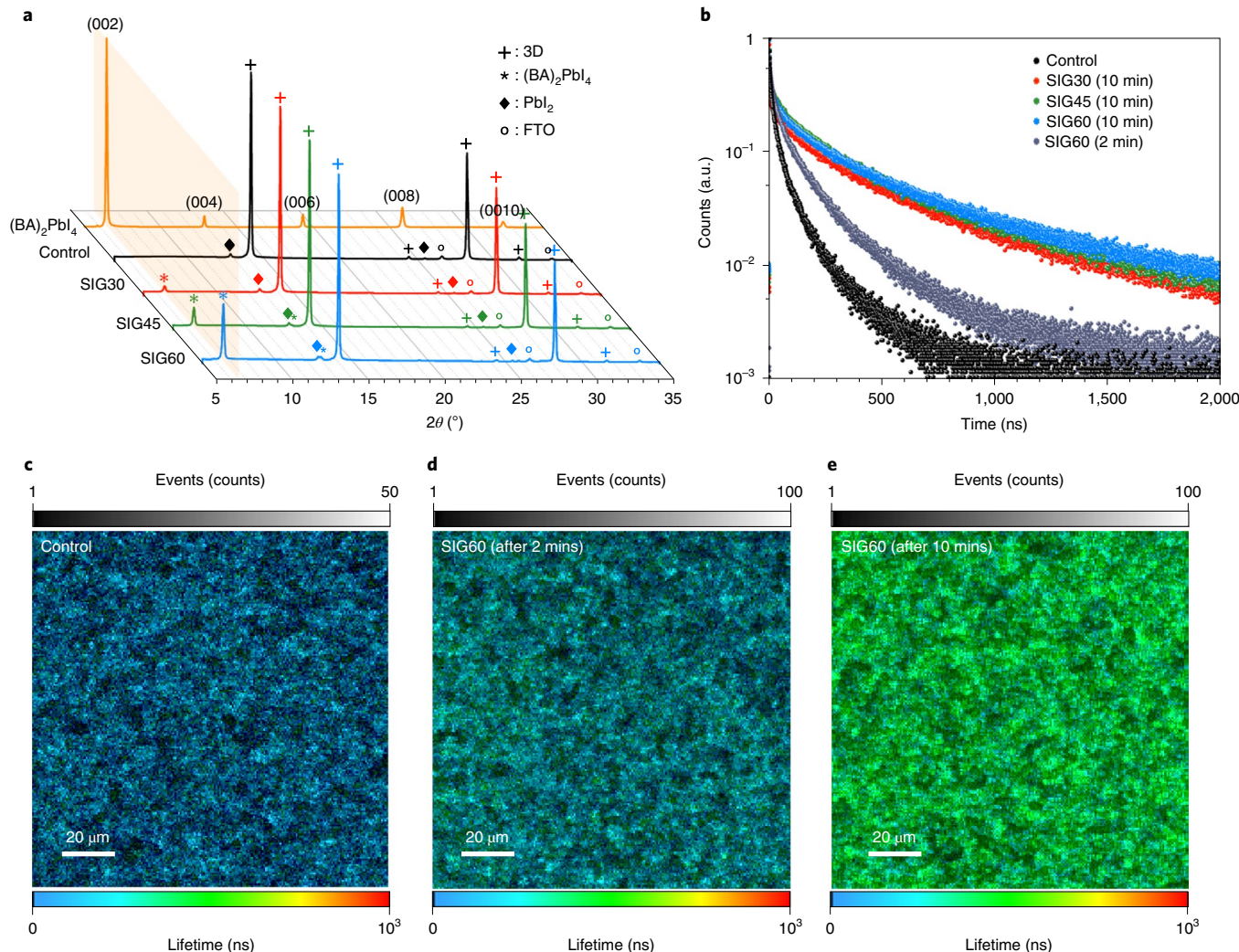


Fig. 2 | Properties of the 2D/3D films fabricated by the SIG method. **a**, X-ray diffraction patterns of the control film (3D perovskite only), 2D/3D films developed by the SIG process under different temperature conditions, and a pure 2D perovskite film ($n=1$, $(\text{BA})_2\text{PbI}_4$). The orange shading indicates 6.4° . **b**, Time-resolved photoluminescence decay curves of the control and SIG-processed 2D/3D films after excitation at 800 nm and 0.5 MHz. **c–e**, Average lifetime mapping images of the 3D perovskite film and 2D/3D films (**c**) after 2 min (**d**) and 10 min (**e**) of processing under SIG60. The colour-scale bars indicate average carrier lifetime whereas the greyscale bars indicate event counts.

grazing-incidence wide-angle X-ray scattering (GIWAXS) images of the control 3D film, the solution-processed (twice) 2D/3D film, and the SIG60-processed (twice) 2D/3D film. As expected, the solution-processed film shows broad peaks, indicating the generation of a quasi-2D with an undefined phase (Fig. 3b). By contrast, our SIG-processed film consistently shows only one sharp peak that corresponds to pure $(\text{BA})_2\text{PbI}_4$ (Fig. 3c). This implies that the target 2D material can be grown on the 3D surface in any desired thickness using repetition of the SIG process. We also observed a uniform and intact 2D/3D bilayer over the entire surface of the SIG film from a slightly tilted cross-sectional SEM image (Fig. 3d).

The electric field distribution at the intact 2D/3D junction is determined by the semiconducting properties (such as the carrier concentration and work function) of the 2D and 3D films. Figure 3e presents the position of each band and work function for 2D and 3D films that were estimated via ultraviolet photoelectron spectroscopy data and the Tauc plot from the ultraviolet-visible absorption spectrum (Supplementary Figs. 8 and 9). Most $(\text{FAPbI}_3)_x(\text{MAPbBr}_3)_{1-x}$ -based perovskites have been reported to be p-type materials^{32,33}, and the 3D perovskite we used exhibited p-type properties in the previous report on Hall

measurements^{6,34}. The ultraviolet photoelectron spectroscopy result also shows that the Fermi level (4.81 eV) of the used 3D perovskite is slightly lower than the midpoint between the CBM (conduction band minimum) of 4.01 eV and VBM (valence band maximum) of 5.56 eV. $(\text{BA})_2\text{PbI}_4$ has also been reported to be a p-type material according to finely controlled scanning Kelvin probe microscopy measurements³⁵. $(\text{BA})_2\text{PbI}_4$ has a wider bandgap of 2.38 eV and a higher work function of 4.92 eV than the corresponding values (1.55 eV and 4.81 eV, respectively) for $(\text{FAPbI}_3)_{0.95}(\text{MAPbBr}_3)_{0.05}$.

The 2D/3D junction can therefore be interpreted as a p-p isotype heterojunction and its band bending is represented in Fig. 3f according to the explanation in Supplementary Fig. 10 and Supplementary Note 3. Formation of a p-p isotype heterojunction is a typical way of inducing a back-surface field at the junction between a wide-bandgap p-type field-induced layer and a narrow-bandgap p-type light-absorbing layer^{36,37}. In the 2D/3D heterojunction, $(\text{BA})_2\text{PbI}_4$ and $(\text{FAPbI}_3)_{0.95}(\text{MAPbBr}_3)_{0.05}$ correspond to the wide-bandgap p-type field-induced material and narrow-bandgap p-type light-absorbing material, respectively. Here the junction must be designed such that sufficient thickness of the field-induced layer is ensured, as when the p-p heterojunction is

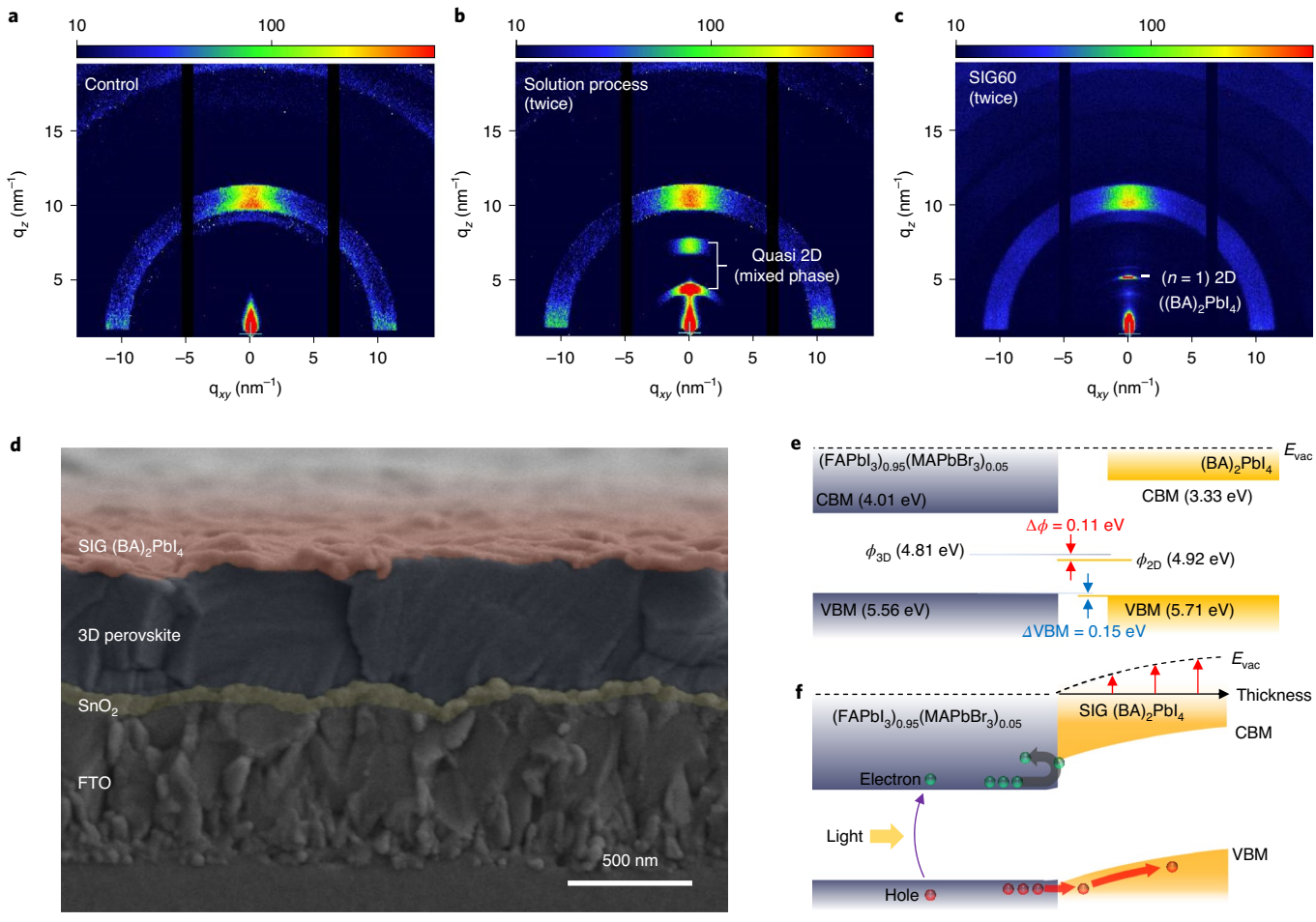


Fig. 3 | Intact 2D/3D heterojunction formation and its role. **a–c**, GIWAXS patterns of the 3D perovskite film (control) (**a**) and 2D/3D perovskites made by two cycles of the solution (**b**) and SIG (**c**) processes. \mathbf{q} is the scattering vector. The colour-scale bars indicate intensity. **d**, A cross-sectional SEM image of the SIG-processed 2D/3D device. **e**, Estimated energy-level alignment between the 3D perovskite and (BA) $_2$ PbI $_4$. ϕ_{2D} and ϕ_{3D} are the Fermi levels of the 2D and 3D perovskites, respectively, $\Delta\phi$ is the Fermi level difference between the 2D and 3D perovskites, E_{vac} is the vacuum level, and ΔVBM is a valence band maximum difference between 2D and 3D perovskites. **f**, Built-in potential change induced by 2D/3D heterojunction formation. The grey and red thick arrows indicate flow of photogenerated holes and photogenerated electrons, respectively, whereas the purple arrow indicates excitation of electron caused by light. The black narrow line represents the thickness change of the 2D perovskite and the orange narrow lines are the vacuum level change caused by it.

formed, the intrinsic hole movement from the field-induced layer to the light-absorbing layer must be sufficient to form a satisfactory back-surface field. The back-surface field can be represented by the built-in potential (V_{bi}) in the depletion region of the wide-bandgap p-type layer. When the wide-bandgap p-type layer is thin enough to be fully depleted, V_{bi} is dependent on the thickness of the wide-bandgap p-type layer, as described in Supplementary Note 3. We estimated the 2D thickness for forming a sufficient depletion region and V_{bi} using Supplementary equation (5) for different carrier concentrations of the 2D layer, and the result is presented in Supplementary Fig. 11. The depletion region depends on the carrier concentration of the 2D layer; however, an increase in the thickness of the 2D layer could augment the additional V_{bi} by further ensuring the depletion region in the 2D layer. A thicker intact 2D layer was therefore expected to provide a higher photovoltaic performance for the PSCs obtained through the SIG process.

Performance and stability of PSCs

Figure 4a shows the current density–voltage (J – V) curves and a summary of the cell parameters, such as the short-circuit current density (J_{sc}), V_{oc} and fill factor for both the control and

SIG60 devices with a FTO/SnO $_2$ /perovskite/spiro-OMeTAD/Au structure (where spiro-OmeTAD is 2,2',7,7'-tetrakis(*N,N*-di-4-methoxyphenylamine)-9,9'-spirobifluorene and FTO is fluorine-doped tin(IV) oxide). The SIG60 device shows considerably improved V_{oc} compared with the control device, thus yielding an improvement in the PCE from 22.39% to 24.59%. It also shows negligible J – V hysteresis and a stabilized power output at the maximum power point (Fig. 4a and Supplementary Fig. 12) and a certified efficiency in terms of the J – V PCE (24.59%; J_{sc} , 24.70 mA cm $^{-2}$; V_{oc} , 1.185 V; fill factor, 83.90%) and quasi-steady-state PCE (24.35%; J_{sc} , 24.83 mA cm $^{-2}$; V_{oc} , 1.173 V; fill factor, 83.59%) without any encapsulation by Newport (Supplementary Fig. 13). As the 2D perovskite layer thickness increased from 0 nm (control) to 40 nm (SIG30) and 80 nm (SIG60), the V_{oc} increased from 1.098 V to 1.117 V and 1.185 V, and the PCE increased gradually (Supplementary Table 4). The J_{sc} values were similar—regardless of the thickness of the SIG-2D film—and were in accordance with the integrated J_{sc} values from the external quantum efficiency spectra (Supplementary Fig. 14). The fill-factor value slightly improved from 82.95% to 83.90% despite an increase in the series resistance from 5.39 to 6.60 Ω cm $^{-2}$ (Supplementary Fig. 15). This implies that the positive

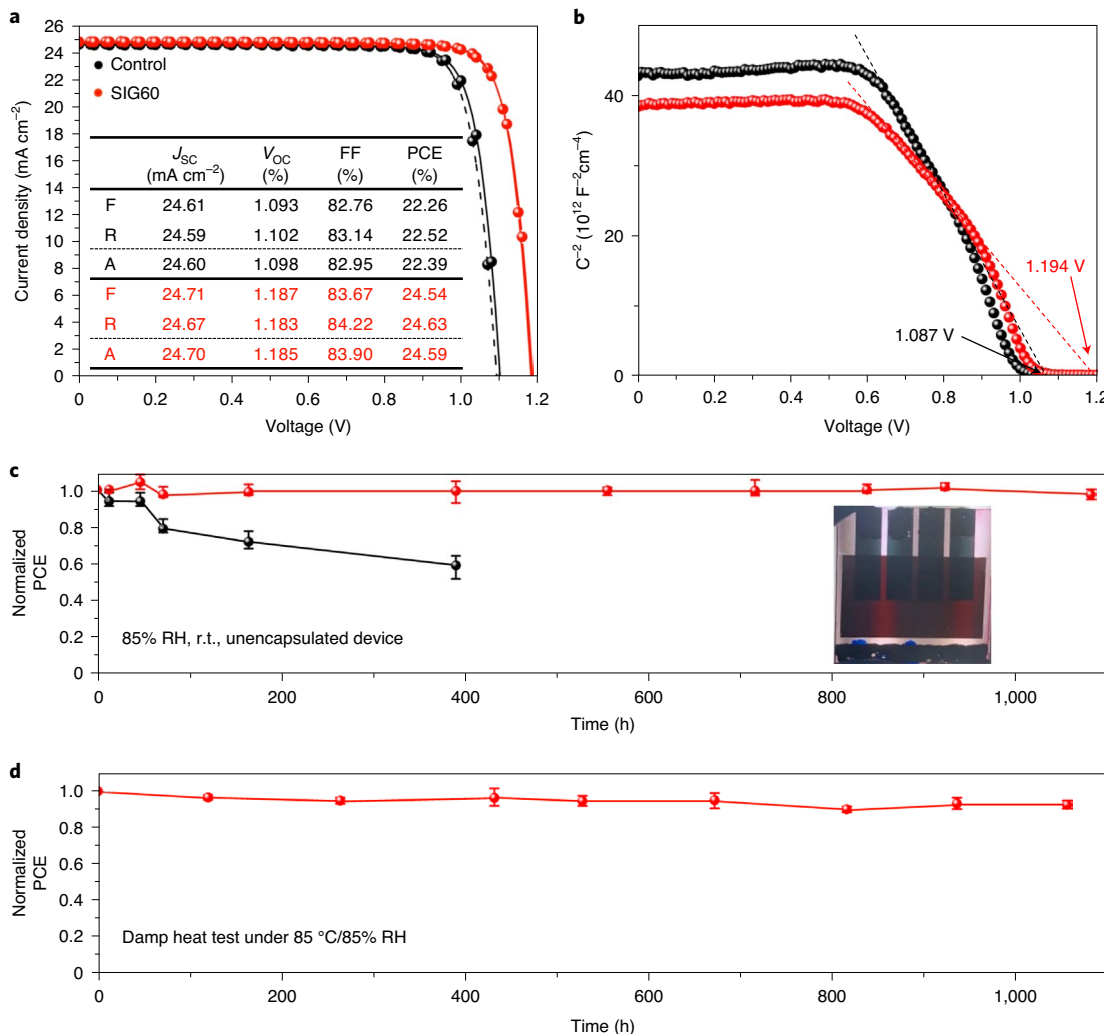


Fig. 4 | Device performance and stability. **a**, A comparison of the photovoltaic performances of the control (FTO/SnO₂/3D/spiro-OMeTAD/Au) and SIG60 (FTO/SnO₂/3D:(SIG-2D)/spiro-OMeTAD/Au) devices. Solid lines and dashed lines indicate the reverse and forward scans, respectively. **b**, Mott-Schottky plots of the control and SIG60 devices (FTO/3D:(SIG-2D)/spiro-OMeTAD/Au) at 10 kHz. Built-in potentials for all devices were obtained by linear fitting derived from Supplementary equation (6). **c**, capacitance. **c**, Efficiency degradation tracking of the unencapsulated control and SIG60 devices under 85% relative humidity (RH) at 25 °C in a dark chamber. The inset in **c** shows the condition of the device after 1,083 h. The initial average efficiency of the four cells are all over 20%. **d**, The results of the 1,056 h thermal stability test of the SIG60 device with encapsulation under 85% RH at 85 °C in the dark. The initial average efficiency of four cells are all over 21.70% The error bars in **c** and **d** show the maximum and minimum bounds of normalized PCEs for four cells. FF, fill factor; F, forward scan; R, reverse scan; A, average; r.t., room temperature.

effect of the surface passivation and the back-surface field of the 2D layer was superior to the negative effect of the series resistance for the fill factor. The statistical data in Supplementary Fig. 16 also show that the improvement of V_{OC} is reproducible and critical for the high PCE of the SIG60 device.

The TRPL results in Fig. 2b indicate that in addition to the reduction of surface recombination, other factors are involved in the V_{OC} improvement. The band bending at the 2D/3D heterojunction in Fig. 3f can have a positive effect on the V_{OC} , similar to the back-surface field of GaAs solar cells. We executed Mott-Schottky plot analysis to confirm the V_{bi} alteration in the SIG device³⁸. The details of the procedure for selecting the parameters are described in Supplementary Fig. 17 and Supplementary Note 4. Reliable Mott-Schottky plots were obtained for control and SIG devices in Supplementary Fig. 18. In Fig. 4b, the Mott-Schottky plots for the control and SIG60 devices show that the introduction of the 2D/3D junction enhances V_{bi} through the SIG process compared with the

control device and the V_{bi} increases from 1.087 V to 1.194 V as the thickness of the 2D layer increases.

Comparing the measured V_{bi} with the V_{OC} for SIG devices in Supplementary Table 5, the increase in V_{OC} has a similar trend to the increase in V_{bi} with increasing 2D thickness despite the similar photoluminescence carrier lifetimes. This result reveals that the V_{bi} obtained by employing the 2D layer was designable by the 2D layer thickness and was critical for V_{OC} enhancement. This result is notable because controllability of the 2D layer thickness on top of the 3D layer has not been demonstrated before. We observed that the calculated V_{bi} values—with a carrier concentration of the 2D layer of $1.67 \times 10^{16} \text{ cm}^{-3}$ —are significantly similar to the differences in the measured V_{bi} and V_{OC} between the control and SIG devices in Supplementary Table 5. This result clearly indicates that the increase in V_{OC} with the thickness of the 2D layer is associated with increasing V_{bi} in that a thicker 2D layer forms a thicker depletion region (Supplementary Fig. 19). Consequently,

the SIG-(BA)₂PbI₄ layer could exhibit a thickness of several tens of nanometres while maintaining its inherent properties such that it enabled an improvement in the device performance. We also confirmed that the V_{bi} provided by the SIG-2D layer worked well for other hole-transporting systems, such as poly(triarylamine) (PTAA) and poly(3-hexylthiophene) (P3HT) (Supplementary Table 6, and Supplementary Figs. 20 and 21).

The SIG device was expected to enhance the resistance against the external environment. The reason is that organic spacers that prevent the penetration of moisture³⁹ and suppress the leak of volatile cations and halides from 3D perovskite film are arranged in the surface direction⁴⁰, and the pure ($n=1$) state has a superior heat resistance to the quasi-2D phases that are usually produced by the solution process. The reactivity with moisture for the control (FTO/SnO₂/3D) and SIG-grown (FTO/SnO₂/3D:SIG-2D) films was estimated by measuring the ultraviolet-visible absorbance before and after exposure to 85% relative humidity and room temperature. Supplementary Fig. 22 shows that the SIG film maintained its absorbance even after 1,000 h, in contrast to the control film. The humidity stability test of the device was also conducted by placing the fabricated devices with undoped P3HT as the HTL in a chamber at 85% relative humidity and room temperature (Fig. 4c). Here, undoped P3HT was used to avoid the effect of hygroscopic additives in spiro-OMeTAD, and the initial device performance is shown in Supplementary Fig. 20. The unencapsulated SIG device (FTO/SnO₂/3D:SIG-2D/P3HT/Au) showed only 2.7% (average) degradation compared with the initial PCE after 1,083 h, whereas the unencapsulated control device (FTO/SnO₂/3D/P3HT/Au) showed 41.4% degradation only after 400 h. We also observed that the unencapsulated SIG device (FTO/SnO₂/3D:SIG-2D/spiro-OMeTAD/Au) stored under an air atmosphere at room temperature in the dark maintained its initial PCE even after 7,000 h.

Figure 4d presents the results from the damp heat test of the SIG device with encapsulation under 85 °C/85% relative humidity. PTAA was used for the damp heat test, and device performance is shown in Supplementary Fig. 21. The most stable encapsulated SIG device (FTO/SnO₂/3D:SIG-2D/PTAA/Au) maintained 95% (on average 93%) of its initial PCE of 21.34% after 1,056 h. The pure 2D phase grown by the SIG process enabled thermal stability that could not be otherwise achieved with the solution process⁴¹. The encapsulated SIG device was tested near the maximum power point under full-sun illumination to explore its long-term operational stability at room temperature (Supplementary Fig. 23). The SIG device maintained >98% of its maximum efficiency (24.06%) for 1,620 h. The intact 2D/3D heterojunction leads to excellent operational stability.

Conclusion

We have developed an SIG strategy that enables the formation of an intact 2D/3D halide junction showing remarkable performance enhancement of PSCs in terms of efficiency and stability. The SIG process allows thickness-controllable deposition of a highly crystalline 2D (BA)₂PbI₄ ($n=1$) layer on top of a 3D layer without any quasi-2D phases ($n>1$). The formed intact 2D/3D halide junction increases the carrier lifetime and enables the design of the local electric field distribution at the junction, yielding a significant improvement to V_{OC} in PSCs. The PSCs with the intact 2D/3D junction show a remarkably improved PCE of 24.59% (a certified quasi-steady-state PCE of 24.35%). The intact 2D ($n=1$) layer not only improves the humidity and thermal stability, but also allows excellent operational stability for PSCs under the 1 sun condition. We anticipate that the SIG strategy will open new avenues for designing halide–halide junctions to improve both the PCE and stability of PSCs.

Methods

Materials. Lead iodide (PbI₂) and lead bromide (PbBr₂) were purchased from the Tokyo Chemical Industry. Methylammonium bromide (MABr), methylammonium

chloride (MACl) and formamidinium iodide (FAI) were purchased from Dyesol. Lead(II) oxide (PbO), butylamine (CH₃(CH₂)₃NH₂), hydriodic acid (HI, 57 wt% in H₂O), hypophosphorous acid solution (H₃PO₂, 50 wt% in H₂O), anhydrous dimethylformamide (DMF), anhydrous dimethylsulfoxide (DMSO), chlorobenzene and acetonitrile were purchased from Sigma-Aldrich. Spiro-OMeTAD was purchased from Lumtec, P3HT was purchased from 1-Material and PTAA was purchased from Mott-Schottky solution.

Synthesis of (BA)₂PbI₄ crystal powder. A mixed solution of HI solution (16 ml) and H₃PO₂ solution (2 ml) was prepared in a 200 ml glass volumetric flask. PbO powder (2,232 mg, 10 mmol) was dissolved by heating to boiling under stirring, and it formed a bright yellow solution; 993 µl (10 mmol) of butylamine was then added to this solution and stirring was discontinued. The temperature was lowered to 80 °C over 30 min. The solution was left at room temperature until orange crystals began to form. The crystals were isolated by suction filtration and thoroughly dried in a vacuum chamber.

(BA)₂PbI₄ perovskite film fabrication. Tin-doped indium oxide (ITO)-coated glass substrates of 2.5 cm × 2.5 cm were cleaned with deionized water, acetone, ethanol and isopropyl alcohol for 15 min each. For better wetting of the 2D perovskite precursor solution, the substrates were treated with ultraviolet-ozone for 15 min; (BA)₂PbI₄ precursor solution was then prepared by dissolving 0.172 g ml⁻¹ (BA)₂PbI₄ crystal powder in DMF/DMSO (8:1 v/v) mixed solvent. The precursor solution was then spin-coated on the substrate at 5,000 r.p.m. for 20 s; 1 ml of diethyl ether was quickly poured onto the substrate at 10 s. The yellow film was quickly transferred to a hot plate and heat-treated at 100 °C for 5 min.

3D perovskite film fabrication. FTO (Pilkington, TEC8) substrates of 2.5 cm × 2.5 cm were cleaned with deionized water, acetone, ethanol and isopropyl alcohol for 15 min each. The substrates were cleaned with ultraviolet-ozone for 15 min and a SnO₂ layer was subsequently grown as the electron transport layer according to a previous report⁴². The substrates were then heat-treated at 150 °C for 1 h. For better wetting of the precursor solution of the 3D perovskite, the FTO/SnO₂ substrates were treated with ultraviolet-ozone for a further 15 min. The 3D perovskite precursor solution was then prepared by mixing 0.869 g ml⁻¹ FAPbI₃, 0.035 g ml⁻¹ MAPbBr₃ and 0.028 g ml⁻¹ MACl in DMF/DMSO (8:1 v/v) mixed solvent. The precursor solution was then coated onto the FTO/SnO₂ substrates by two consecutive spin-coating steps at 1,000 r.p.m. and 5,000 r.p.m. for 5 s and 30 s, respectively; 1 ml of diethyl ether was quickly poured onto the substrate at 10 s after reaching 5,000 r.p.m. The yellow film was quickly transferred to a hot plate and heat-treated at 150 °C for 10 min.

SIG process. A hot-press method was used to fabricate the 3D/SIG-2D film. The previously fabricated (BA)₂PbI₄ thin film was placed on the 3D thin film and pressed at 60 MPa for 10 min at the desired temperature (30 °C, 45 °C or 60 °C). For the purpose of analysing the growth of the SIG-processed 2D film under different pressures, 3D/SIG-2D thin films were made by changing the pressure (20 MPa, 40 MPa or 60 MPa) at 60 °C.

Hole transport layer and counter electrode fabrication. Spiro-OMeTAD solution (1.1 mg ml⁻¹ in chlorobenzene) with the addition of 23 µl of bis(trifluoromethanesulfonyl)imide (Li-TFSI) (540 mg ml⁻¹ in acetonitrile), 10 µl of cobalt-TFSI (375 mg ml⁻¹ in acetonitrile) and 39 µl of 4-tertbutylpyridine was spin-coated on the substrate coated with FTO/SnO₂/3D/(SIG-2D) at 2,000 r.p.m. for 30 s. Undoped P3HT solution (10 mg ml⁻¹ in the mixed solvent chlorobenzene:diphenyl ether = 97:3 v/v) was used for the humidity stability test, whereas PTAA solution (12 mg ml⁻¹ in toluene) with the addition of 6 µl of Li-TFSI (340 mg ml⁻¹ in acetonitrile) and 6 µl of 4-tertbutylpyridine was used for the damped heat test. Finally, a gold counter electrode was deposited by thermal evaporation; the active area of the counter electrode was fixed at 0.16 cm².

Material and film characterization. X-ray diffraction spectra were measured using a Rigaku SmartLab X-ray diffractometer with an X-ray tube (copper K α , $\lambda=1.54\text{ \AA}$, 200 mA, 45 kV, 9 kW). All of the XRD patterns were measured under a scan rate of 1° per min with a step of 0.02° at the National Center for Inter-university Research Facilities at Seoul National University. Plan-view and cross-sectional SEM images were obtained by using a field-emission scanning electron microscope (MERLIN, Carl Zeiss). A cross-section view near the 2D/3D heterojunction was observed using a transmission 200 kV field-emission electron microscope (JEOL, JEM-2100F). A TRPL study was performed using an inverted-type scanning confocal microscope (MicroTime-200, Picoquant) with a $\times 40$ (air) objective. Lifetime measurements were performed at the Korea Basic Science Institute, Daegu Center. A single-mode pulsed diode laser (32.7 µJ cm⁻²; 470 nm with a pulse width of ~30 ps, a laser power of ~0.1 µW, a repetition rate of 0.5 MHz and an effective confocal area of $6.11 \times 10^{-9}\text{ cm}^2$; ref. ⁴³) was used as an excitation source. A dichroic mirror (490 DCXR, AHF), a 75 µm pinhole and a single-photon avalanche diode (PDM series, MPD) were used to collect emission from the samples. The time-correlated single-photon counting technique was used to count emission photons. Time-resolved photoluminescence images consisting

of 200×200 pixels were recorded using the time-tagged time-resolved data acquisition method and the exponential fitting of the obtained photoluminescent decays was performed using Symphotime-64 software (version 2.2), according to the method used in ref.⁴³. GIWAXS patterns were obtained from the Wide Angle X-ray Scattering Spectrometer (XEUSS2.0, Xenocs at National Instrumentation Center for Environmental Management at Seoul National University. The X-ray wavelength was 1.54 \AA and the incidence angle of the X-ray was set to 0.1° . Two-dimensional GIWAXS data were recorded with a DECTRIS hybrid pixel photon counting detector.

Device characterization. To estimate the solar cell performance, photovoltaic cells were measured using a solar simulator (Newport, Oriel ClassAAA, 94043 A) with a source meter (Keithley 2420) of 100 mA cm^{-2} under AM 1.5 G illumination and a calibrated silicon reference cell certificated by NREL; $J-V$ curves were obtained in the forward and reverse directions from -0.2 V to 1.2 V and measured at 100 mV s^{-1} and 10 mV step intervals. The photovoltaic performance measurements were performed at room temperature under air. The devices were covered with a metal mask to set the active area to 0.094 cm^2 . The external quantum efficiency was measured from 320 nm to 900 nm at an interval of 5 nm (QuantX-300, Newport). For Mott–Schottky analysis, capacitance–voltage measurements were carried out at a fixed frequency (10 kHz) (IviumStat, IVIUM TECHNOLOGIES). A Mott–Schottky plot was obtained in the forward direction from -0.2 V to 1.2 V . The active area of the counter electrode was calibrated to 0.16 cm^2 .

Device stability testing. For continuous humidity stability tests, an unencapsulated device was stored in a thermo hygrostat chamber (TH-PE, JEIO TECH) with 85% relative humidity at 25°C . The photovoltaic performance of the aged devices was measured under ambient conditions. Encapsulation was performed to measure the stability under 85% relative humidity at 85°C . The SIG device and glass cover were attached using ultraviolet induced resin in a N_2 glove box. The stability test under 85% relative humidity at 85°C was then carried out in the chamber. The long-term operational stability test was performed with a current and voltage monitor (INA219, Adafruit) under an AM 1.5 G simulated white LED (LSH-7320, Newport). The long-term operation test system was operated by a self-customized program.

Reporting Summary. Further information on research design is available in the Nature Research Reporting Summary linked to this article.

Data availability

All data generated or analysed during this study are included in the published article and its Supplementary Information and Source Data. Source data are provided with this paper.

Received: 21 April 2020; Accepted: 20 November 2020;
Published online: 4 January 2021

References

- Best Research-Cell Efficiencies (NREL, 2020); <https://www.nrel.gov/pv/assets/pdfs/best-research-cell-efficiencies.20200708.pdf>
- Green, M. A. et al. Solar cell efficiency tables (version 56). *Prog. Photovolt. Res. Appl.* **28**, 629–638 (2020).
- Liu, Y. et al. Ultrahydrophobic 3D/2D fluoroarene bilayer-based water-resistant perovskite solar cells with efficiencies exceeding 22%. *Sci. Adv.* **5**, eaaw2543 (2019).
- Cho, K. T. et al. Water-repellent low-dimensional fluorous perovskite as interfacial coating for 20% efficient solar cells. *Nano Lett.* **18**, 5467–5474 (2018).
- Yoo, J. J. et al. An interface stabilized perovskite solar cell with high stabilized efficiency and low voltage loss. *Energy Environ. Sci.* **12**, 2192–2199 (2019).
- Jung, E. H. et al. Efficient, stable and scalable perovskite solar cells using poly(3-hexylthiophene). *Nature* **567**, 511–515 (2019).
- Hu, Y. et al. Hybrid perovskite/perovskite heterojunction solar cells. *ACS nano* **10**, 5999–6007 (2016).
- Cho, Y. et al. Mixed 3D–2D passivation treatment for mixed-cation lead mixed-halide perovskite solar cells for higher efficiency and better stability. *Adv. Energy Mater.* **8**, 1703392 (2018).
- Lu, J. et al. Diammonium and monoammonium mixed-organic-cation perovskites for high performance solar cells with improved stability. *Adv. Energy Mater.* **7**, 1700444 (2017).
- Jeon, N. J. et al. A fluorene-terminated hole-transporting material for highly efficient and stable perovskite solar cells. *Nat. Energy* **3**, 682–689 (2018).
- Shin, S. S. et al. Colloidally prepared La-doped BaSnO_3 electrodes for efficient, photostable perovskite solar cells. *Science* **356**, 167–171 (2017).
- Yoon, H., Kang, S. M., Lee, J.-K. & Choi, M. Hysteresis-free low-temperature-processed planar perovskite solar cells with 19.1% efficiency. *Energy Environ. Sci.* **9**, 2262–2266 (2016).
- Tsai, H. et al. High-efficiency two-dimensional Ruddlesden–Popper perovskite solar cells. *Nature* **536**, 312–316 (2016).
- Beznosikov, B. & Aleksandrov, K. Perovskite-like crystals of the Ruddlesden–Popper series. *Crystallogr. Rep.* **45**, 792–798 (2000).
- Ortiz-Cervantes, C., Carmona-Monroy, P. & Solis-Ibarra, D. Two-dimensional halide perovskites in solar cells: 2D or not 2D? *ChemSusChem* **12**, 1560–1575 (2019).
- Quan, L. N. et al. Ligand-stabilized reduced-dimensionality perovskites. *JACS* **138**, 2649–2655 (2016).
- Wang, Z. et al. Efficient ambient-air-stable solar cells with 2D–3D heterostructured butylammonium–caesium-formamidinium lead halide perovskites. *Nat. Energy* **2**, 17135 (2017).
- Li, P. et al. Phase pure 2D perovskite for high-performance 2D–3D heterostructured perovskite solar cells. *Adv. Mater.* **30**, 1805323 (2018).
- Ma, C. et al. 2D/3D perovskite hybrids as moisture-tolerant and efficient light absorbers for solar cells. *Nanoscale* **8**, 18309–18314 (2016).
- Leng, K. et al. Molecularly thin two-dimensional hybrid perovskites with tunable optoelectronic properties due to reversible surface relaxation. *Nat. Mater.* **17**, 908–914 (2018).
- Xiao, J. et al. Pressure-assisted $\text{CH}_3\text{NH}_3\text{PbI}_3$ morphology reconstruction to improve the high performance of perovskite solar cells. *J. Mater. Chem. A* **3**, 5289–5293 (2015).
- Chen, H. et al. A solvent-and vacuum-free route to large-area perovskite films for efficient solar modules. *Nature* **550**, 92–95 (2017).
- Cao, D. H., Stoumpos, C. C., Farha, O. K., Hupp, J. T. & Kanatzidis, M. G. 2D Homologous perovskites as light-absorbing materials for solar cell applications. *JACS* **137**, 7843–7850 (2015).
- Porter, D. A. & Easterling, K. E. *Phase Transformations in Metals and Alloys (Revised Reprint)* Ch. 4 (CRC, 2009).
- Li, R. et al. Gibbs–Curie–Wulff theorem in organic materials: a case study on the relationship between surface energy and crystal growth. *Adv. Mater.* **28**, 1697–1702 (2016).
- Chen, P. et al. In situ growth of 2D perovskite capping layer for stable and efficient perovskite solar cells. *Adv. Funct. Mater.* **28**, 1706923 (2018).
- Lin, Y. et al. Unveiling the operation mechanism of layered perovskite solar cells. *Nat. Commun.* **10**, 1–11 (2019).
- Zhao, B. et al. High-efficiency perovskite–polymer bulk heterostructure light-emitting diodes. *Nat. Photon.* **12**, 783–789 (2018).
- Stolterfoht, M. et al. Visualization and suppression of interfacial recombination for high-efficiency large-area pin perovskite solar cells. *Nat. Energy* **3**, 847–854 (2018).
- Tress, W. Perovskite solar cells on the way to their radiative efficiency limit—insights into a success story of high open-circuit voltage and low recombination. *Adv. Energy Mater.* **7**, 1602358 (2017).
- Tai, M. et al. In situ formation of a 2D/3D heterostructure for efficient and stable CsPbI_2Br solar cells. *J. Mater. Chem. A* **7**, 22675–22682 (2019).
- Chen, Y. et al. Strain engineering and epitaxial stabilization of halide perovskites. *Nature* **577**, 209–215 (2020).
- Kim, H. et al. Optimal interfacial engineering with different length of alkylammonium halide for efficient and stable perovskite solar cells. *Adv. Energy Mater.* **9**, 1902740 (2019).
- Gunawan, O. et al. Carrier-resolved photo-Hall effect. *Nature* **575**, 151–155 (2019).
- Zhang, F. et al. Complexities of contact potential difference measurements on metal halide perovskite surfaces. *J. Phys. Chem. Lett.* **10**, 890–896 (2019).
- Galiana, B., Rey-Stolle, I., Baudrit, M., García, I. & Algara, C. A comparative study of BSF layers for GaAs-based single-junction or multijunction concentrator solar cells. *Semicond. Sci. Technol.* **21**, 1387 (2006).
- Chen, H. L. et al. A 19.9%-efficient ultrathin solar cell based on a 205-nm-thick GaAs absorber and a silver nanostructured back mirror. *Nat. Energy* **4**, 761–767 (2019).
- Almora, O., Aranda, C., Mas-Marzá, E. & García-Belmonte, G. On Mott–Schottky analysis interpretation of capacitance measurements in organometal perovskite solar cells. *Appl. Phys. Lett.* **109**, 173903 (2016).
- Quintero-Bermudez, R. et al. Compositional and orientational control in metal halide perovskites of reduced dimensionality. *Nat. Mater.* **17**, 900–907 (2018).
- Schlipf, J. et al. Shedding light on the moisture stability of 3D/2D hybrid perovskite heterojunction thin films. *ACS Appl. Energy Mater.* **2**, 1011–1018 (2019).
- Sutanto, A. A. et al. Dynamical evolution of the 2D/3D interface: a hidden driver behind perovskite solar cell instability. *J. Mater. Chem. A* **8**, 2343–2348 (2020).
- Anaraki, E. H. et al. Highly efficient and stable planar perovskite solar cells by solution-processed tin oxide. *Energy Environ. Sci.* **9**, 3128–3134 (2016).
- Kim, S.-Y. et al. Excitation dynamics of $\text{MAPb}(\text{I}_{1-x}\text{Br}_x)_3$ during phase separation by photoirradiation: evidence of sink, band filling, and Br-rich phase coarsening. *J. Alloy. Compd.* **806**, 1180–1187 (2019).

Acknowledgements

This work was supported by the National Research Foundation of Korea (NRF) grant funded by the Korea government (MSIP) (grant nos. NRF-2020R1A2C3009115, NRF-2017M1A2A2087351 (the Technology Development Program to Solve Climate Changes); NRF-2017R1A4A1015022) and the New and Renewable Energy Core Technology Program of the Korea Institute of Energy Technology Evaluation and Planning (KETEP) from the Ministry of Trade, Industry and Energy (grant no. 20183010014470). This work was also supported by the Global Frontier R&D Program of the Center for Multiscale Energy Systems funded by the National Research Foundation under the Ministry of Education, Science and Technology, Korea (grant no. 2012M3A6A7054855). The authors thank S.-j. Park (Korea I.T.S.; XRD instrumental broadening calculation), W.-S. Chae (Korea Basic Science Institute; TRPL mapping) for their help during the course of the study.

Author contributions

Y.-W.J., S.L., M.C. and J.H.N conceived the idea and interpreted the data. Y.-W.J. and S.L. shaped and optimized the SIC process. Y.-W.J. synthesized and analysed 2D perovskite powder and film. S.L. and Y.-W.J. performed the fabrication and characterization of the PSCs with support from K.M.Y. and K.C. S.L. and Y.-W.J. estimated the long-term

stability of films and devices with encapsulation by K.J. All authors participated in the discussion. Y.-W.J., S.L., M.C. and J.H.N. wrote the manuscript. J.H.N. and M.C. supervised this project.

Competing interests

The authors declare no competing interests.

Additional information

Supplementary information is available for this paper at <https://doi.org/10.1038/s41560-020-00749-7>.

Correspondence and requests for materials should be addressed to M.C. or J.H.N.

Peer review information *Nature Energy* thanks Pablo Docampo, Wanyi Nie and the other, anonymous, reviewer(s) for their contribution to the peer review of this work.

Reprints and permissions information is available at www.nature.com/reprints.

Publisher's note Springer Nature remains neutral with regard to jurisdictional claims in published maps and institutional affiliations.

© The Author(s), under exclusive licence to Springer Nature Limited 2021

Solar Cells Reporting Summary

Nature Research wishes to improve the reproducibility of the work that we publish. This form is intended for publication with all accepted papers reporting the characterization of photovoltaic devices and provides structure for consistency and transparency in reporting. Some list items might not apply to an individual manuscript, but all fields must be completed for clarity.

For further information on Nature Research policies, including our [data availability policy](#), see [Authors & Referees](#).

► Experimental design

Please check: are the following details reported in the manuscript?

1. Dimensions

Area of the tested solar cells

- Yes
 No

We used a mask with 0.094 cm^2 (circle type) for measuring photovoltaic performance. The area values can be found in the method section

Explain why this information is not reported/not relevant.

Method used to determine the device area

- Yes
 No

The area of our masks was determined by observing optical microscope and certified at Newport corporation.

Explain why this information is not reported/not relevant.

2. Current-voltage characterization

Current density-voltage (J-V) plots in both forward and backward direction

- Yes
 No

The J-V plots measured along both scan direction is shown in Figure 4a, Supplementary Fig. 20, and Supplementary Fig. 21.

Explain why this information is not reported/not relevant.

Voltage scan conditions

For instance: scan direction, speed, dwell times

- Yes
 No

For unit cell, bias between -0.2 V and 1.2 V was applied for measurement of J-V curves along forward and backward (we used terminology as 'reverse') scan direction. The step voltage and scan speed were fixed at 10 mV and 100 mV/s, respectively.

Explain why this information is not reported/not relevant.

Test environment

For instance: characterization temperature, in air or in glove box

- Yes
 No

Our devices were characterized at room temperature (ca. 25 Celsius degree) in air.

Explain why this information is not reported/not relevant.

Protocol for preconditioning of the device before its characterization

- Yes
 No

To prevent reflection of incident light, anti-reflection film was attached on glass side in the case of measurement of unit cells.

Explain why this information is not reported/not relevant.

Stability of the J-V characteristic

Verified with time evolution of the maximum power point or with the photocurrent at maximum power point; see ref. 7 for details.

- Yes
 No

Stability of efficiency at maximum power point can be found in Supplementary Figure 12.

Explain why this information is not reported/not relevant.

3. Hysteresis or any other unusual behaviour

Description of the unusual behaviour observed during the characterization

- Yes
 No

No J-V hysteresis of SIG device was observed and the related comments were mentioned in manuscript.

Explain why this information is not reported/not relevant.

Related experimental data

- Yes
 No

Above values could be verified from Figure 4a.

Explain why this information is not reported/not relevant.

4. Efficiency

External quantum efficiency (EQE) or incident photons to current efficiency (IPCE)

- Yes
 No

The EQE spectrum can be found in Supplementary Figure 13 and Figure 14.

Explain why this information is not reported/not relevant.

A comparison between the integrated response under the standard reference spectrum and the response measure under the simulator

- Yes
 No

The comparison is represented in Figure 4a and Supplementary Figure 14.

Explain why this information is not reported/not relevant.

For tandem solar cells, the bias illumination and bias voltage used for each subcell

- Yes
 No

State where this information can be found in the text.

Our devices were only fabricated for single-junction solar cells.

5. Calibration

Light source and reference cell or sensor used for the characterization

Yes
 No

We measured using a solar simulator (Newport, Oriel Class A, 94043A) with a sourcemeter (Keithley 2420) of 100 mA/cm^2 under illumination at AM 1.5G and Si-reference cell.

Explain why this information is not reported/not relevant.

Confirmation that the reference cell was calibrated and certified

Yes
 No

We used a calibrated Si-reference cell certificated by NREL.

Explain why this information is not reported/not relevant.

Calculation of spectral mismatch between the reference cell and the devices under test

Yes
 No

The spectral mismatch factor was determined by PV Lab of Technology and Application Center in Newport Corporation and we applied the value in our laboratory.

Explain why this information is not reported/not relevant.

6. Mask/aperture

Size of the mask/aperture used during testing

Yes
 No

We used a mask with 0.094 cm^2 (circle type) for measuring photovoltaic performance. The area values can be found in the method section

Explain why this information is not reported/not relevant.

Variation of the measured short-circuit current density with the mask/aperture area

Yes
 No

State where this information can be found in the text.
The J_{sc} value for our device was confirmed through the Newport Corporation measurement.

7. Performance certification

Identity of the independent certification laboratory that confirmed the photovoltaic performance

Yes
 No

Our devices were certified at PV Lab of Technology and Application Center in Newport Corporation.

Explain why this information is not reported/not relevant.

A copy of any certificate(s)

Provide in Supplementary Information

Yes
 No

A copy of certificates can be found in Supplementary Figure 13.

Explain why this information is not reported/not relevant.

8. Statistics

Number of solar cells tested

Yes
 No

For statistical analysis of efficiencies, 28 devices were tested.

Explain why this information is not reported/not relevant.

Statistical analysis of the device performance

Yes
 No

The statistical data was represented in Supplementary Figure 16.

Explain why this information is not reported/not relevant.

9. Long-term stability analysis

Type of analysis, bias conditions and environmental conditions

For instance: illumination type, temperature, atmosphere humidity, encapsulation method, preconditioning temperature

Yes
 No

For humidity test, unencapsulated devices had been kept in a chamber of 85% relatively humidity and 25 Celsius degree under dark. And photovoltaic performances of the devices were measured in air. The data can be found in Figure 4c. Thermal stability test had been performed at 85 Celsius degree and ca. 85% relatively humidity in dark. The data can be found in Figure 4d. For long term stability test in Supplementary Figure 23, encapsulated device was exposed under AM 1.5G simulated with white LED.

Explain why this information is not reported/not relevant.

Solar Cells Reporting Summary

Nature Research wishes to improve the reproducibility of the work that we publish. This form is intended for publication with all accepted papers reporting the characterization of photovoltaic devices and provides structure for consistency and transparency in reporting. Some list items might not apply to an individual manuscript, but all fields must be completed for clarity.

For further information on Nature Research policies, including our [data availability policy](#), see [Authors & Referees](#).

► Experimental design

Please check: are the following details reported in the manuscript?

1. Dimensions

Area of the tested solar cells

Yes
 No

We used a mask with 0.094 cm^2 (circle type) for measuring photovoltaic performance. The area values can be found in the method section

Explain why this information is not reported/not relevant.

Method used to determine the device area

Yes
 No

The area of our masks was determined by observing optical microscope and certified at Newport corporation.

Explain why this information is not reported/not relevant.

2. Current-voltage characterization

Current density-voltage (J-V) plots in both forward and backward direction

Yes
 No

The J-V plots measured along both scan direction is shown in Figure 4a, Supplementary Fig. 20, and Supplementary Fig. 21.

Explain why this information is not reported/not relevant.

Voltage scan conditions

For instance: scan direction, speed, dwell times

Yes
 No

For unit cell, bias between -0.2 V and 1.2 V was applied for measurement of J-V curves along forward and backward (we used terminology as 'reverse') scan direction. The step voltage and scan speed were fixed at 10 mV and 100 mV/s, respectively.

Explain why this information is not reported/not relevant.

Test environment

For instance: characterization temperature, in air or in glove box

Yes
 No

Our devices were characterized at room temperature (ca. 25 Celsius degree) in air.

Explain why this information is not reported/not relevant.

Protocol for preconditioning of the device before its characterization

Yes
 No

To prevent reflection of incident light, anti-reflection film was attached on glass side in the case of measurement of unit cells.

Explain why this information is not reported/not relevant.

Stability of the J-V characteristic

Verified with time evolution of the maximum power point or with the photocurrent at maximum power point; see ref. 7 for details.

Yes
 No

Stability of efficiency at maximum power point can be found in Supplementary Figure 12.

Explain why this information is not reported/not relevant.

3. Hysteresis or any other unusual behaviour

Description of the unusual behaviour observed during the characterization

Yes
 No

No J-V hysteresis of SIG device was observed and the related comments were mentioned in manuscript.

Explain why this information is not reported/not relevant.

Related experimental data

Yes
 No

Above values could be verified from Figure 4a.

Explain why this information is not reported/not relevant.

4. Efficiency

External quantum efficiency (EQE) or incident photons to current efficiency (IPCE)

Yes
 No

The EQE spectrum can be found in Supplementary Figure 13 and Figure 14.

Explain why this information is not reported/not relevant.

A comparison between the integrated response under the standard reference spectrum and the response measure under the simulator

Yes
 No

The comparison is represented in Figure 4a and Supplementary Figure 14.

Explain why this information is not reported/not relevant.

For tandem solar cells, the bias illumination and bias voltage used for each subcell

Yes
 No

State where this information can be found in the text.

Our devices were only fabricated for single-junction solar cells.

5. Calibration

Light source and reference cell or sensor used for the characterization

Yes
 No

We measured using a solar simulator (Newport, Oriel Class A, 94043A) with a sourcemeter (Keithley 2420) of 100 mA/cm^2 under illumination at AM 1.5G and Si-reference cell.

Explain why this information is not reported/not relevant.

Confirmation that the reference cell was calibrated and certified

Yes
 No

We used a calibrated Si-reference cell certificated by NREL.

Explain why this information is not reported/not relevant.

Calculation of spectral mismatch between the reference cell and the devices under test

Yes
 No

The spectral mismatch factor was determined by PV Lab of Technology and Application Center in Newport Corporation and we applied the value in our laboratory.

Explain why this information is not reported/not relevant.

6. Mask/aperture

Size of the mask/aperture used during testing

Yes
 No

We used a mask with 0.094 cm^2 (circle type) for measuring photovoltaic performance. The area values can be found in the method section

Explain why this information is not reported/not relevant.

Variation of the measured short-circuit current density with the mask/aperture area

Yes
 No

State where this information can be found in the text.
The J_{sc} value for our device was confirmed through the Newport Corporation measurement.

7. Performance certification

Identity of the independent certification laboratory that confirmed the photovoltaic performance

Yes
 No

Our devices were certified at PV Lab of Technology and Application Center in Newport Corporation.

Explain why this information is not reported/not relevant.

A copy of any certificate(s)
Provide in Supplementary Information

Yes
 No

A copy of certificates can be found in Supplementary Figure 13.

Explain why this information is not reported/not relevant.

8. Statistics

Number of solar cells tested

Yes
 No

For statistical analysis of efficiencies, 28 devices were tested.

Explain why this information is not reported/not relevant.

Statistical analysis of the device performance

Yes
 No

The statistical data was represented in Supplementary Figure 16.

Explain why this information is not reported/not relevant.

9. Long-term stability analysis

Type of analysis, bias conditions and environmental conditions

For instance: illumination type, temperature, atmosphere humidity, encapsulation method, preconditioning temperature

Yes
 No

For humidity test, unencapsulated devices had been kept in a chamber of 85% relatively humidity and 25 Celsius degree under dark. And photovoltaic performances of the devices were measured in air. The data can be found in Figure 4c. Thermal stability test had been performed at 85 Celsius degree and ca. 85% relatively humidity in dark. The data can be found in Figure 4d. For long term stability test in Supplementary Figure 23, encapsulated device was exposed under AM 1.5G simulated with white LED.

Explain why this information is not reported/not relevant.

